Geometric Perturbation of Dielectric Resonator for Multifunctional MIMO Application

Taomia Tasnuba Pramiti

A Thesis

in

The Department

of

Electrical and Computer Engineering

Presented in Partial Fulfillment of the Requirements

for the Degree of Master of Applied Science at

Concordia University

Montreal, Quebec, Canada

October, 2017

This is to certify that the thesis prepared

By: Taomia Tasnuba Pramiti

Entitled: Geometric Perturbation of Dielectric Resonator for Multifunctional MIMO Application

and submitted in partial fulfillment of the requirements for the degree of

Master of Applied Science

Complies with the regulations of this University and meets the accepted standards with respect to originality and quality.

Signed by the final examining committee:

_____ Chair
      Dr. R. Raut

_____ Examiner, External
      Dr. Marco Bertola(Mathematics)   To the Program

_____ Examiner
      Dr. Abdel R. Sebak

_____ Examiner
      Dr. Shamseldien

_____ Supervisor
      Dr. Ahmed Kishk

Approved by: _____
           Dr. W. E. Lynch, Chair
      Department of Electrical and Computer Engineering

_____20_____   _____
                        Dr. Amir Asif, Dean
              Faculty of Engineering and Computer Science

Abstract

One of the recent concepts in communication systems is Multiple Input Multiple Output (MIMO) that has the potential to improve channel capacity by utilizing multiple transmitters and receivers. However, to reduce the implication on the required radiating element footprint, multiple antennas should be replaced with a single antenna that provides orthogonal multiple radiation patterns associated with the feeding ports. In addition, the proper use of frequency spectrum is possible when different modes of an antenna can be excited at the same frequency with polarization and radiation pattern orthogonality.

This work proposes the idea of combining the multifunction device and multimode antenna with a dielectric resonator for a single band operation. The geometry of a cylindrical dielectric resonator has been perturbed to combine the radiating $TM_{01\delta}$ and $HEM_{11\delta}$ modes with the non-radiating mode $TE_{01\delta}$ at the same frequency. The methodology of tuning several modes of DR with coupling mechanism and several practical concerns is mentioned in this work. The effect and rationalization of the introduced geometry perturbation parameters are presented. A prototype of the introduced concept is designed, fabricated and measured to prove the concept targeting the Wi-Fi MIMO applications. Afterwards, the designed device is used as a single element in a cascaded two element design where four different antennas work simultaneously at a single frequency with a filter. In summary, the main contributions of this work are: presenting the detailed procedure of geometry perturbation, including the metal placement on top of the resonator; proposing a coupling mechanism for tuning modes for simultaneous excitation; validating the introduced concept and methodology with a comparison between a simulated and measured prototype designed for MIMO applications; cascading two elements to obtain four independent antennas incorporating a filter.

Contents

List of Figures

List of Tables

Chapter 1

Introduction

One of the critical limitations of mobile communication performance is the multi-path propagation of the electromagnetic waves. When there is no direct line of sight path between transmitter and receiver (especially in the urban areas where many obstacles are present), receiver collects reflected, scattered, and diffracted signals. These signals follow multiple paths of different lengths resulting in time and spatial displacement from one another. The receiver combines these signals having a random phase and amplitude variation that causes fluctuation in signal strength. This phenomenon is known as fading and responsible for severe losses of the signal such as distortion, time dispersion, random frequency modulation, etc. [1]. To combat the channel fading, the concept of multiple antennas has been introduced to increase diversity, which is known as Multiple Input Multiple Output (MIMO) system [2], [3].

1.1 MIMO antennas

The MIMO system employs multiple antennas at both the transmitting and receiving ends. A transmitted signal sends through different paths, and the receiver combines multiple independently faded replicas of the signal that improves the signal quality by providing maximal gain diversity and ensures reliability [1]. On the other hand, by establishing pairs between each transmitting and receiving antenna, multiple parallel spatial channels can be well defined that carry independent information. Thus, MIMO provides the advantage of spatial multiplexing to increase data rates [4]. Therefore, MIMO takes advantage from fading signals and multipath delayed signals for multiplying transfer rates and improves the magnitude of the signal without any additional cost for spectrum [2]. Fig. 1-1 shows the MIMO wireless communication system where the transmitter and receiver are equipped with N and M antennas, respectively, and Table 1-I represents the evolution of MIMO technology through different standards.
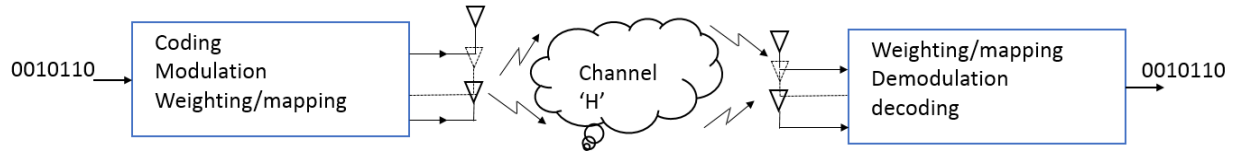
Fig. 1-1: MIMO Wireless transmission system of N transmitters and M receivers [2].

Table 1-I: MIMO system comparison between different IEEE standards [6].

IEEE standard	802.11b	802.11g/a	802.11n	802.11ac
Maximum data rate per stream (Mb/s)	11	55	>100	>500
Frequency Band (GHz)	2.4/5	2.4 and 5	2.4 and 5	5
Channel width(MHz)	20	20/40	20 and 40	20,40,80,16,80-80
Antenna technology	Single Input Single Output(SISO)	SISO	Multiple Input Multiple Output(MIMO)	MU-MIMO
Transmission Technique	Direct Sequence Spread Spectrum(DSSS)	DSSS and Orthogonal Frequency Division Multiplexing(OFDM)	OFDM	OFDM
Maximum number of spatial streams	1	1	4	8
Beamforming capable	No	No	Yes	Yes
Date ratified by IEEE	1999	2003/1999	2009	2013

The performance of MIMO system depends on the antenna specifications such as array gain, diversity gain, spatial multiplexing gain, and interference reduction [5]. Therefore, antenna selection plays a significant role in the MIMO performance. Based on the throughput and quality-of-service requirements of different applications, the combination of diversity and multiplexing should be chosen carefully. In addition, the antenna element correlation in an array environment should be low. Otherwise high correlation between adjacent elements causes pattern distortion that leads to low capacity. This can be done when each antenna element has a unique response to each multipath component depending on the arrival phase due to the antenna location (spatial diversity) or magnitude and phase due to the antenna pattern (angle diversity) or polarization diversity [3].

The conventional MIMO system has an implication on the required radiating element footprint, which is the main challenge in such design. One attractive solution, in this case, is replacing multiple antennas with a single antenna that provides orthogonal multiple radiation patterns associated with the feeding ports [7]. This is how the concept of Multimode antenna is introduced where orthogonal modes of a single antenna are excited to obtain both polarization diversity and pattern diversity. On the other hand, proper use of frequency spectrum is possible when different modes of an antenna can be excited at the same frequency with polarization and pattern variations. This is also another challenge to have degenerated modes with the various patterns at the same frequency. Furthermore, Massive MIMO technology is invented for the secure, robust, energy and spectrum efficient future broadband network. This system consists of antenna arrays of few hundred antennas to serve many tens of terminals at the same time-frequency resource [8].

1.2 Multifunctional device

Modern communication systems require compact size multifunctional devices under controlled operating conditions such as the frequency band, interference, traffic patterns, etc. The notion of multi-function came in front to miniaturize RF modules. The rapid downsizing of the mobile terminals demands compact devices that can operate in the same or multiple frequency bands for several applications, especially the RF front-end devices such as antenna, filter, ballun, etc. To serve this purpose a similar approach as mentioned in preceding MIMO section, excitation of multi-modes in a single structure is a perfect solution. Multiple modes of a resonating structure can achieve the goals of multifunction operating at different frequencies. The functions of these devices can be multi-polarized antennas, filter, oscillator, power combiner, diplexer, etc. and depending on the requirements of applications some of these can be realized using different modes [9], [10]. By combining various functions together, it is possible to reduce volume, weight as well as losses because of additional connections between multiple devices. However, a design challenge here is having multiple applications operating at the same frequency to obtain spectrum efficiency.

1.3 Motivation

As the compactness is a very critical factor in mobile devices, so the concept of having multiple applications in the same device is an extensive way of miniaturization. In addition, advancement of the wireless communication demands efficient utilization of the scarce RF spectrum. Therefore, to save the high cost of the frequency spectrum, it is beneficial to operate different applications at the same frequency. To achieve both compactnesses as well as spectral efficiency, one unique solution could be including the MIMO antennas in a multi-functional device operating in a single band, which is the motivation of this thesis. Achieving these features all together requires different modes of the material to resonate at the same frequency, which is not possible naturally and leads to some modifications to shift the resonance frequencies of modes. This necessity of shifting modes introduced the idea of geometry perturbation to change the effective permittivity at the boundaries that cause a change in the frequencies of the modes inside material [11], [12]. The perturbation method assumes that the total fields inside the cavity do not vary much compared to the unperturbed cavity. This perturbation can be done by shape change

or insertion of dielectric/ metallic material in the cavity that causes small variation in the field distribution and tunes the resonant frequencies of the modes.

In case of perturbation, Dielectric resonators are being used for several decades [13], [14]. The three-dimensional structure of dielectric resonator provides more degrees of freedom to have several orthogonal modes inside and gives more options for a perturbation to bring various modes at the same frequency. Also, the high radiation efficiency, wide impedance matching bandwidth, and compact size of the DRA make it a perfect applicant for MIMO applications [15]. Therefore, DR can be exploited to achieve the goal of a single band multifunctional device consisting of MIMO antennas through geometry perturbation.

1.4 Objectives

The objective of the thesis is rigorously perturbing the geometry of a canonical DR to have the three lower order modes $TE_{01\delta}$, $TM_{01\delta}$ and $HEM_{11\delta}$ operating at the same frequency. Depending on the electric and magnetic field distribution as well as the electric and magnetic energies of the modes, perturbation areas should be chosen carefully. Although perturbation of the DR is the most crucial part of the work, the excitation of three modes also needs more attention as three different techniques are required based on applications. Especially, shielding plays an important role when used as a filter. Finally, the perturbed DR can be utilized for many applications such as filter, oscillator, broadside antenna, omnidirectional antenna, etc.

1.5 Outline of the Thesis

This thesis is organized into five chapters. The literature review chapter provides information about the pioneers of DRAs as well as some relevant works on DRAs for multifunctional use and MIMO applications. This chapter also mentions some useful researches about perturbation of dielectric resonators. Chapter 3 'Perturbation of DRA' introduces the details of DR modes perturbation techniques. Field and energy distributions of the modes are provided to explain perturbations. Furthermore, the perturbation concept used in this chapter is applied to design a multifunctional device for Wi-Fi applications. The detailed procedure of excitation of different modes is given in chapter four. Simulation and measurement plots are provided to validate the concept. The designed structure of chapter four is used as a single element in a cascaded two-element device in chapter five to obtain four independent antennas for MIMO applications incorporating a filter. Finally, chapter six gives the conclusions and some future work ideas.

Chapter 2
Literature Review

This chapter represents some of the published works of the researchers about Dielectric resonators related to multifunctional device and MIMO antennas. Although a considerable number of researchers have successfully proven, their contribution to DR works. Few pioneers have shown the roadmap to others. Here some of the iconic pioneers' names are mentioned. In addition, as the perturbation is one of the essential parts of this thesis, few related types of research on perturbation of dielectric resonators are specified with relevant figures.

2.1 Pioneers of dielectric resonator

Dielectric resonator antenna has become an emerging technology over the last four decades. The use of dielectric resonator was first introduced as microwave resonator in 1939 by Richtinger, and the modes of dielectric resonators were first analyzed by Okaya and Barash [16]. S. B. Cohn is one of the pioneers who adopted the feature of obtaining high-quality factor because of the high dielectric constant of resonators for circuit applications [17]. To maintain high Q factors, dielectric resonators are often enclosed in metal cavities that prevent radiation.

However, these same dielectric resonators can be used as an antenna by removing the shielding, and this idea was implemented by S Long, M. McAllister and L. Shen in early 1980s [18]. The successful implementation of dielectric resonators as an antenna element influenced other researchers, especially Birand and Gelsthorpe to design a first linear array and Haneishi and Takazawa to demonstrate the first planar array in the 1980s [18]. These researchers showed that the dielectric resonators could be considered as an alternative to the conventional low gain antennas such as monopole, dipole or microstrip antennas.

The exponential growth of the dielectric resonator is visible after the significant contributions of three groups in the early 1990s in realizing feeding mechanism, applying numerical and analytical techniques to calculate the Q factor and input impedances. Among these three groups, one group was led by Kishk and Glisson; another was led by Luk and Leung, the last one was led

by Mongia [19]. A remarkable work done by Mongia and Bhartia is presented in [20] that describes the mode nomenclature of DR and equations to calculate resonant frequency and Q factors of various modes. Furthermore, there are so many researchers who have significant efforts for the development of Dielectric resonator in the areas of compact designs, wideband designs, tunable dielectric resonator antennas, reconfigurable patterns and much more.

2.2 Dielectric resonator as multifunctional device

Modern communication systems require compact size multifunctional devices under controlled operating conditions such as the frequency band, interference, and traffic patterns [21]. Dielectric resonators (DRs) can serve the purpose as multifunctional devices by using their different modes simultaneously for various functions. Intensive research has been done on DR to act as a multifunctional device from last decade, but the concept of using multiple modes of DR was implemented a few decades ago. In early 80's, Guillon et al. presented that in a cylindrical dielectric resonator a number of degenerate modes with identical natural frequencies can be coupled together to form coupled circuits [13]. For reducing the size of the filters and equalizers, degenerated dual hybrid modes are used in [22] where a triple mode DR was proposed in [23] for a high power, and stable temperature filter using TM_{110} modes. In the later stage, a considerable number of works are published based on dual and triple modes of DR.

Afterwards, at the end of the last decade, the use of dielectric as a packaging material inspired Lim et al. to study the dual functionality of a hollow DR as an antenna and a packaging cover [26]. In the same year, Laila et al. utilized the application of both high and low Q factor of DR in the same structure as an oscillator and a radiating element [24]. After that, a dual functional DR device consisting of an antenna and a filter are shown in [27], and a dual polarized antenna with both vertical and horizontal polarizations was proposed in [25]. Afterwards, several applications exploited the ability of dielectric resonator for not only dual functions, but for three applications simultaneously [28], [10].

However, to save spectrum cost, some research groups explored various techniques to perturb the resonant frequencies of different modes of the dielectric resonators to operate at the same frequency [23], [29]. Various methods were implemented for frequency tuning such as

using screws, irises, corner cuts [30], etc. Moreover, the dielectric resonator became an attractive subject for multifunctional applications for a long time.

2.3 Perturbation of dielectric resonator

Perturbation of microwave cavity resonators is a well-established technique for a long time that has been reviewed in a mid-20th-century literature [31]. However, perturbation of dielectric resonators found in early 80's when Guillon et al. showed the use of tuning screws to tune $TE_{01\delta}$ mode and to couple orthogonal HE_{111} modes of DR [13]. In case of material measurement, there was a problem with a conventional perturbation technique where the signal source was much stable and determining sensitivity was critical. A solution of this problem is illustrated in [32] by using a semi-open dielectric resonator sandwiched between two metal plates that allow a small, low loss dielectric sample to be appropriately inserted and determines the permittivity of the sample rapidly. This technique worked adequately for the small materials that have permittivity in between 2 to 38.

Tremendous works have been done on perturbation of DR to operate it as an oscillator, filter, and diplexer. To improve the stability of an oscillator and to control its modes, a high Q sapphire dielectric ring whispering gallery mode resonator is proposed as a discriminator in [33]. A switchable bandpass filter is presented in [34] using dielectric perturbation where a piezoelectric transducer lifts up or pulls down the dielectric perturbed to turn on or off the DR filter. In [35] two cylindrical cavities loaded with triple mode dielectric resonators are employed as a diplexer for base station applications. Instead of a traditional corner cuts perturbation or screws perturbation, an off-centered dielectric resonator perturbs the two degenerate modes in the diplexer.

In addition, extensive research works are published about the contribution of DR perturbation on improving antenna performance. A perturbation technique of a microstrip-fed cylindrical DRA to reduce cross-polarization from higher order $HEM_{01\delta}$ mode is elaborated in [37]. As the electric field of $HEM_{01\delta}$ is strong at the center, a cavity of different ϵr is inserted and found the best cross-polarization level for air cavity. By removing two dielectric pieces from a rectangular DRA, an A-shaped DRA is formed to afford broader impedance matching, better broadside

pattern and reduced weight [36]. The application of DR perturbation has been found in the investigation of mutual coupling in the reflectarray environment using Finite Difference Time Domain (FDTD) modeling [38].

2.4 Dielectric resonator for MIMO application

For MIMO application more than one signal transmit and receive. When multiple antennas operate at the same frequency, high coupling affects the antenna performance. DRA can be used in this case to get better radiation efficiency as it can transmit and receive more than one signal simultaneously. Reduction of mutual coupling in DRAs is proposed by incorporating it with monopole and patch antennas for WLAN application or by using metasurface shielding between DRAs for 60 GHz band [39], [40].

A comparison between monopole antenna array, patch antenna array and a six-port dielectric resonator antenna array is shown in [41]. The proposed DRA array has spatial, polarization and angular diversities exploit all possible degrees of freedom with the compact size of the antenna that is applicable for the MIMO indoor environment. A reconfigurable pattern compact multiband DRA for portable mobile devices is presented in [42] that provides better correlation and diversity gain. In MIMO system correlation between different antennas is a critical issue that controls the performance of the system. The advantage of using DRA is its decorrelation between the various ports to improve the channel capacity [43]. For LTE base station MIMO application DRA is a perfect option as it is possible to increase the number of degenerated modes applying boundary application maintaining better coupling and SNR [14]. However, to fulfill the demands of the future MIMO communication system, several works are done on DRAs to enhance gain with the reconfigurable pattern, making wideband, millimeter wave array and so on [44], [45].

Chapter 3

Perturbation of DRA

Generally, the modes inside dielectric resonators (DR) do not coincide with the same frequency. Hence, to induce degenerate modes shape perturbation is needed. The cylindrical dielectric resonator is chosen to have more degrees of freedom to design. It is characterized by radius R_{DR}, height H_{DR}, and dielectric constant ϵ_r as shown in Fig. 3-1. The permittivity of $\epsilon_r = 10.2$ is used considering the design cost and its availability. The characteristics of the dielectric resonator depend on the material permittivity ϵ_r as the DR size is proportional to $\lambda_0 / \sqrt{\epsilon_r}$ where λ_0 is free space wavelength [46]. Three lower order modes $TE_{01\delta}$, $HEM_{11\delta}$ and $TM_{01\delta}$ of the DR of $\epsilon_r = 10.2$ are examined. Here, the resonator is placed on top of a substrate of $\epsilon_r = 2.2$ to obtain $TE_{01\delta}$ mode. Otherwise, the $TE_{011+\delta}$ mode will be found if the resonator is directly placed on the ground.
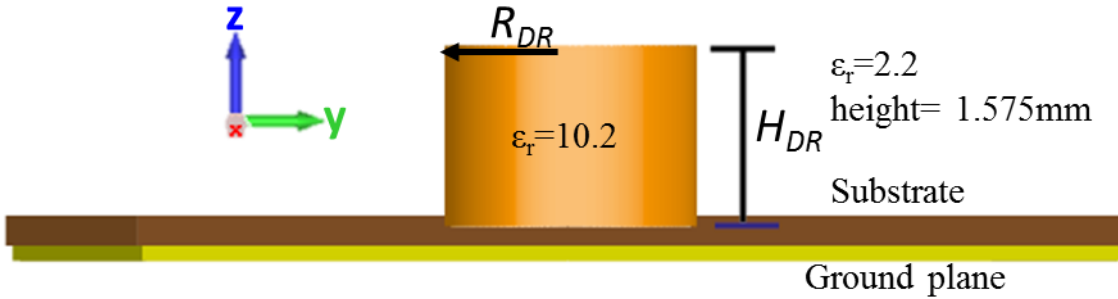
Fig. 3-1: **C**ylindrical Dielectric Resonator [16].

The energy distribution inside the resonator changes with the aspect ratio (R_{DR}/H_{DR}) as it controls the k_0a and quality factor (Q_0). The relation between k_0a and (Q_0) of different modes with respect to aspect ratio can be found in various books [16], [46]. The resonant frequencies of the DR modes are calculated from the above-mentioned parameters. Thus, it is essential to notice the characteristics of the modes with different aspect ratios. Here, the effect of aspect ratio on the frequency changes of the unperturbed DR modes is observed to have an assumption about the required initial dimension of the DR. It is noteworthy that the analysis is done only on the specific permittivity $\epsilon_r = 10.2$.

3.1 Modes behavior with different aspect ratios of unperturbed DR

The electric and magnetic energy concentrations for three possible cases of aspect ratios are described.

- radius = height ($R_{DR} = H_{DR}$)
- radius < height ($R_{DR} < H_{DR}$)
- radius > height ($R_{DR} > H_{DR}$)

(a)   (b)   (c)
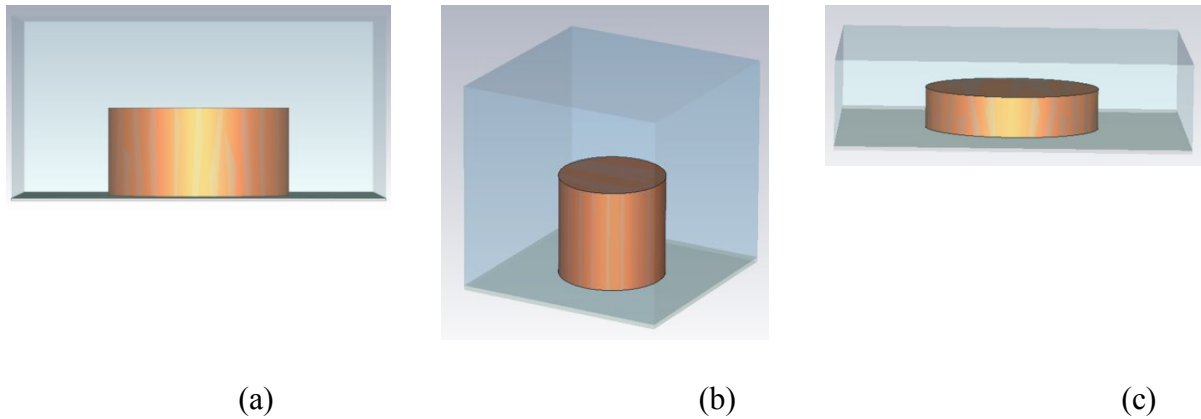
Fig. 3-2: Dielectric Resonators inside a metallic cavity (a) $R_{DR} = H_{DR}$, (b) $R_{DR} < H_{DR}$, and (c) $R_{DR} > H_{DR}$.

The possible configurations are shown in Fig. 3-2. The analysis is done using the Eigenmode Solver of CST [47]. The DR is placed on a substrate of ϵ_r=2.2 (length, l_{sub}=width, w_{sub}=3.75h, thickness, h_{sub}=1.575 mm) and the structure is enclosed in a metallic cavity as shown in Fig. 3-2. The same cavity size is maintained in all cases, and the behavior of the modes has been observed. It should be noted that the cavity size is a critical factor to change the resonance frequency and order of modes. DR initial height (H_{DR}) and radius (R_{DR}) are $0.57\lambda_g$ at any arbitrarily chosen frequency f_n. The frequency f_n is selected arbitrarily because the objective is just to observe the point of aspect ratio where three modes have closest values, and their energy distribution is strong enough to couple to it. The cavity height is chosen to be two times of the

DR height H_{DR} whereas cavity length and width is same as the substrate length and width. The normalized frequency response of different modes with a radius over height ratio is shown in Fig. 3-3.
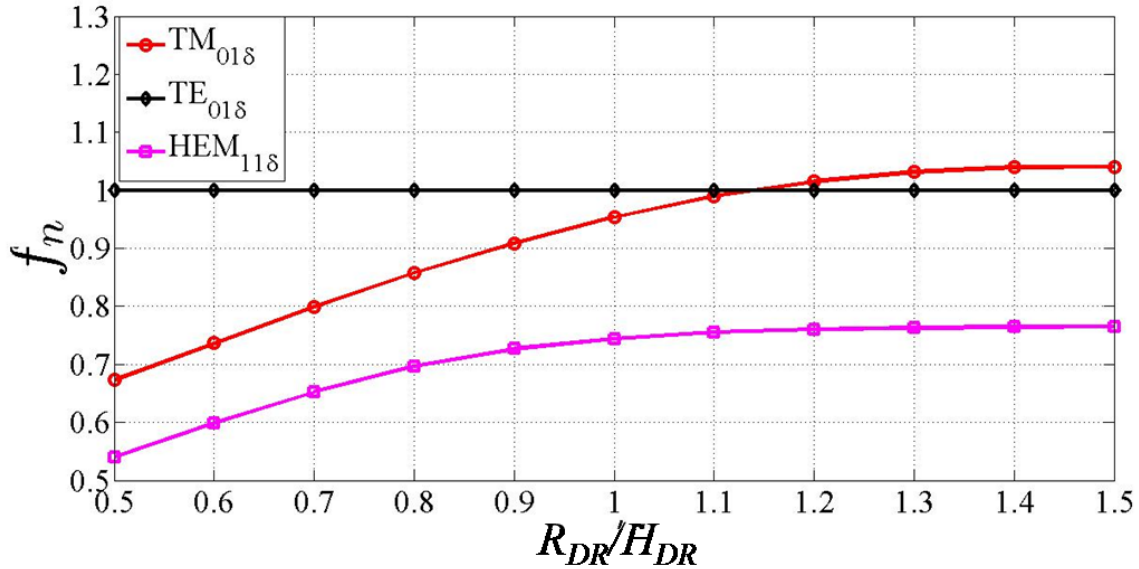
Fig. 3-3: R_{DR}/H_{DR} ratio effect on normalized frequency response (normalized with $TE_{01\delta}$ mode frequency) of different modes.

The values in Fig. 8 are normalized with the $TE_{01\delta}$ mode frequency found for each ratio. However, as the ratio increases, natural frequencies for all the modes decreases, which are not visible in this figure as it is normalized. It is clearly visible that none of the aspect ratios could provide three modes at a single band. When $R_{DR}/H_{DR} = 1.1$ gives $TE_{01\delta}$ and $TM_{01\delta}$ modes at the same frequency, but the $HEM_{11\delta}$ mode is always lower than others. Therefore, it is mandatory to perturb the structure to shift them towards a single frequency band.

From a practical perspective, it is easier to fix one mode at a specific frequency and then changing the geometry to bring other modes at that frequency. In this case, the $TE_{01\delta}$ mode is chosen to be fixed at any particular frequency. It should be noted that perturbing the geometry will not only affect one specific mode but also shifts other modes to some extent. Therefore, it is worth to keep some frequency difference among three modes before initiating perturbation. Here, $R_{DR}/H_{DR} = 1$ has been selected to provide more freedom to geometry perturbation.

3.2 Identifying perturbation area

The precondition of perturbation is finding the suitable area in field and energy distributions where a small change can control the resonance frequency of the modes. The electric field of the $TE_{01\delta}$ mode is equally distributed throughout the resonator except near the substrate part. On the ground, according to the boundary condition, the tangential electric field must be zero. Hence the overall height and radius ratio (R_{DR}/H_{DR}) of the resonator is an important parameter to shift the $TE_{01\delta}$ mode frequency to a specific value f_1.

After fixing $TE_{01\delta}$ mode to the required frequency, one way to perturb the $HEM_{11\delta}$ mode is changing the effective permittivity of the DR region where $HEM_{11\delta}$ mode energy is strong. This can be done by reducing some area of the resonator that changes the effective ϵ_r of DR as the air permittivity is incorporating with the resonator. Thus, it is essential to do the analysis on the field and energy of the modes to locate the perturbation area.

3.2.1 Field and Energy Distributions of different modes inside DR

Another importance of noticing the field and energy distribution is to distinguish between resonating and radiating modes of the DR. Also it is noteworthy that more than one $TM_{01\delta}$ mode exists in the structure as the DR is confined in a cavity. Therefore, to differentiate between the cavity modes and the resonator modes, energy distributions of the modes must be considered. Cavity modes energies leak outside while resonator modes energies are confined inside the DR. The electric and magnetic field distribution of the $HEM_{11\delta}$, $TE_{01\delta}$ and $TM_{01\delta}$ modes for the first context $R_{DR}=H_{DR}$ is displayed in Fig. 3-4, Fig. 3-5, and Fig 3-6.

(a)   (b)   (c)

Fig. 3-4**:** Side view of electric field distributions, (a) $HEM_{11\delta}$, (b) $TE_{01\delta}$, and (c) $TM_{01\delta}$ modes when $R_{DR}=H_{DR}$
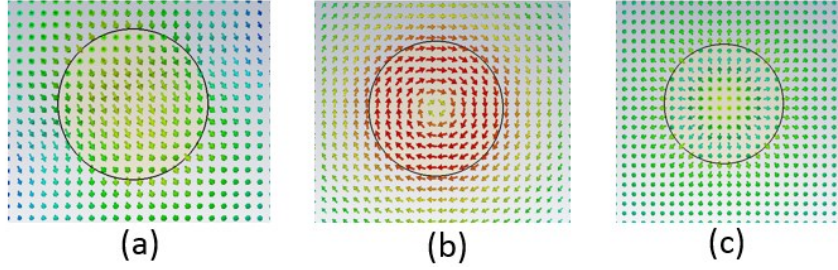
Fig. 3-5: Top view of electric field distributions (a) $HEM_{11\delta}$, (b) $TE_{01\delta}$, and (c) $TM_{01\delta}$ modes when $R_{DR}=H_{DR}$
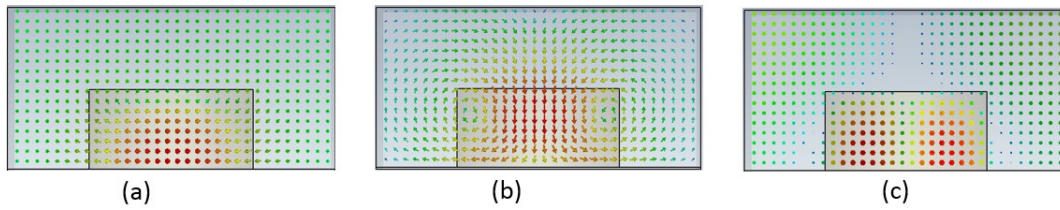
Fig. 3-6: Magnetic field distributions (a) $HEM_{11\delta}$, (b) $TE_{01\delta}$, and (c) $TM_{01\delta}$ modes when $R_{DR}=H_{DR}$
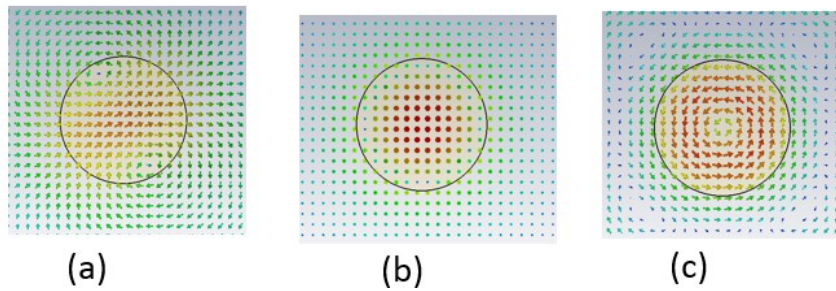
Fig. 3-7: Top view of magnetic field distributions (a) $HEM_{11\delta}$, (b) $TE_{01\delta}$, and (c) $TM_{01\delta}$ modes when $R_{DR}=H_{DR}$

Considering the first situation, the radius is equal to the height of the resonator; the electric energy of $HEM_{11\delta}$ mode is maximum at the top part of the DR and also at the lower edges of the resonator. The electric energy of $TE_{01\delta}$ mode is distributed throughout the resonator and minimum near the substrate area whereas for $TM_{01\delta}$ mode electric energy is mainly concentrated at the center of the resonator. Fig. 3-8 demonstrates the electric energy inside the resonator. Similar energy distributions can be found for any other aspect ratios.
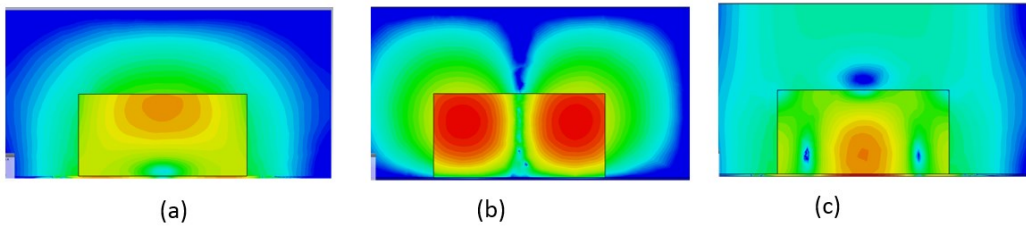
Fig. 3-8: Electric Energy distribution (a) $HEM_{11\delta}$ (b) $TE_{01\delta}$ and (c) $TM_{01\delta}$ modes when $R_{DR}=H_{DR}$

The arrangement of magnetic energies of these three modes for $R_{DR}=H_{DR}$ is also displayed in Fig. 3-9. It is notable that the magnetic energies for all three modes are perfectly confined inside the DR. The electric and magnetic energy distributions in three aspect ratio cases look alike for all three modes of interest.
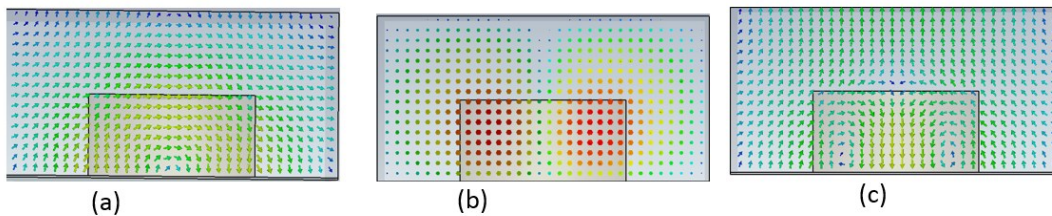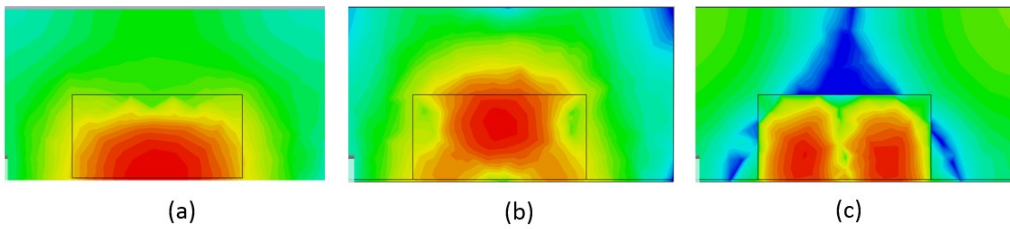

Fig. 3-9: Magnetic Energy distributions (a) $HEM_{11\delta}$ (b) $TE_{01\delta}$ and (c) $TM_{01\delta}$ modes when $R_{DR}=H_{DR}$

3.3 Geometry Perturbation of Dielectric Resonator

The following perturbation process has been illustrated in three steps where the first step illustrates reducing some portion of the bottom part, the second step defines the importance of placing a metal on top of DR, and the third stage is perturbing the top part of the resonator. Each step describes the reason for doing perturbation of that specific area and the details of the perturbation. Fig. 3-10 shows the perturbed dielectric resonator to obtain three different modes at the same frequency.
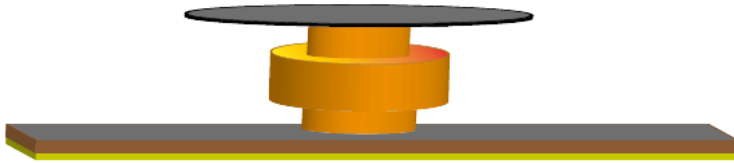
Fig. 3-10: perturbed DR to bring three modes at the same frequency

3.3.1 Perturbing the bottom part of the resonator

As the strong electric field of the $HEM_{11\delta}$ mode is orthogonal to the bottom edges of the resonator thus by removing some portion of the bottom edges can shift the frequency up. The reason behind choosing this area is because the other modes do not have high-intensity electric energy in this position, so they are not affected by this perturbation. However, the $TE_{01\delta}$ mode frequency can be shifted if the height of the perturbed area is large enough to reach the strong electric field concentration of the $TE_{01\delta}$ mode. Therefore, the height of the bottom cut must be chosen carefully. Considering the bottom part height is H_{p1} and radius is r_{p1}. To make the explanation more convenient, normalized values are used. Normalized perturbation height of the bottom area, $h_{p1} = \frac{H_{p1}}{H_{DR}}$ normalized perturbation radius is $r_{p1} = \frac{R_{p1}}{R_{DR}}$ and normalized frequency f_n. The normalized resonant frequency, f_n, of the three modes is shown in Fig. 3-11 with respect to h_{p1} while keeping r_{p1} fixed. To begin, small perturbation responses can be determined using the exact cavity perturbation equations [49].

$$\frac{\omega - \omega_0}{\omega_0} = \frac{\int_{v_0} \Delta\epsilon \,(E_0)^2 + \Delta\mu (H_0)^2}{-\int_{v_0} \epsilon \,(E_0)^2 + \mu (H_0)^2}$$

16

The above equation calculates the shift in resonance frequency due to a small perturbation. The numerator presents the total electric and magnetic energy in the perturbed volume whereas the denominator presents total electric and magnetic energy inside the cavity. To use this equation resonator is placed inside a metallic cavity as shown in Fig. 3-11(a) and calculated the total energy from the full wave solver. This total energy inside the cavity goes to the denominator of the above equation, and numerical method is used to calculate frequency shift for different perturbed volume where h_{p1} and r_{p1} are the tuning parameters to shift f_n.
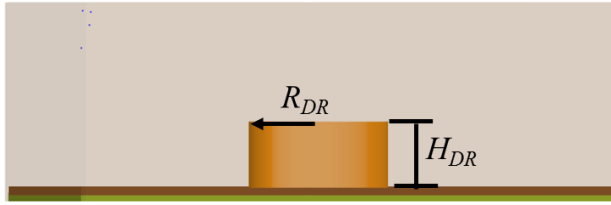
Fig. 3-11(a): Dielectric resonator inside metallic cavity
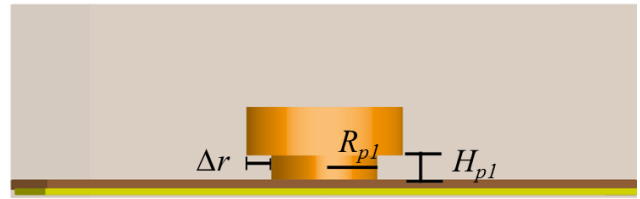
Fig. 3-11(b): Dielectric resonator perturbation inside cavity

$HEM_{11\delta}*$, $TM_{01\delta}*$, and $TE_{01\delta}*$ modes represent the normalized frequencies calculated from the cavity perturbation technique in Fig. 3-12. These equations are usually considered for small perturbations which can be seen from the figure also. Δr presents the change in the normalized bottom radius. In Fig. 3-12, Δr is 0.03 which means a tiny part of DR has been perturbed and then tuned h_{p1} to shift the resonance frequencies. It is noticeable for perturbation at the bottom part, mainly $HEM_{11\delta}$ mode frequency is changing. However, when h_{p1} is more than 0.05 $TM_{01\delta}$ mode also starts to shift.
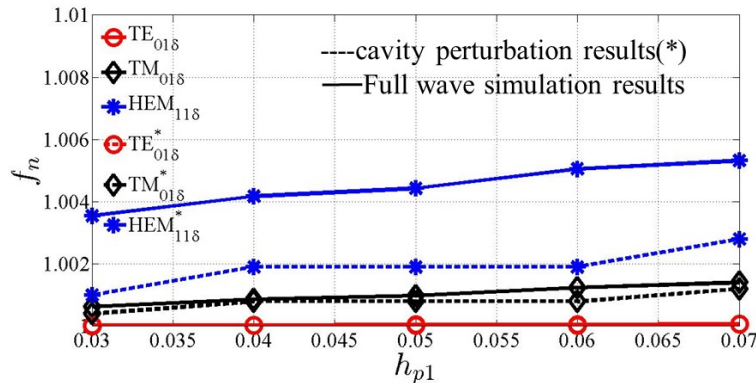
Fig. 3-12: Normalized frequency response with normalized bottom height when $\Delta r=0.03$

To check this technique more precisely, comparatively more significant part is altered and different ε_r DR has been tested. Fig. 3-13 shows the frequency responses of three modes when $\Delta r=0.1$ for $\varepsilon_r=10.2$ which is more significant than the previous example. Values of h_{p1} also varied in a wide range from 0.07 to 0.25. It is clear that $HEM_{11\delta}$ is the most effected mode. However, the $TM_{01\delta}$ mode is also affected but not much. Also, about 2% discrepancy can be seen between cavity perturbation and full wave simulated results when h_{p1} is 0.25.
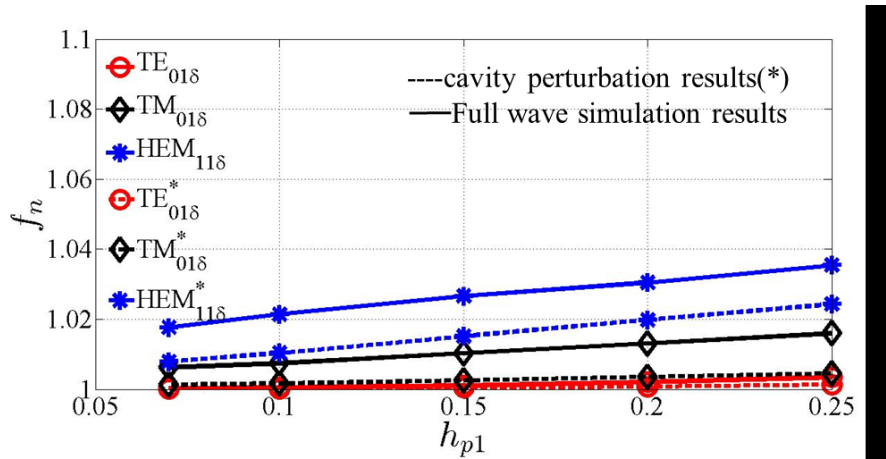
Fig. 3-13: Normalized frequency response with normalized bottom height when $\Delta r=0.1$
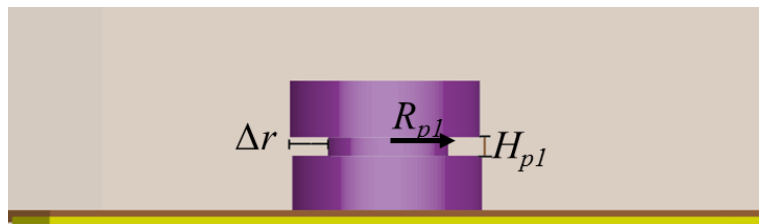
Fig. 3-14: Perturbed dielectric resonator $\varepsilon_r=35$ inside the metallic cavity

Similar perturbation has been done on DR of $\varepsilon_r=35$ with $\Delta r=0.1$. To shift the $TE_{01\delta}$ mode, the middle section of the DR has been perturbed as shown in Fig. 3-14. The normalized height h_{p1} of the perturbation region is varied and the frequency response provided in Fig. 3-15. Although $TE_{01\delta}$ mode shifts up, the $TM_{01\delta}$ mode is the most effected mode here. It is because $TM_{01\delta}$ mode has strong radial field components in the perturbed area which shifts this mode up. These examples show the usability of cavity perturbation technique to select the perturbation area and to estimate the amount of perturbation.
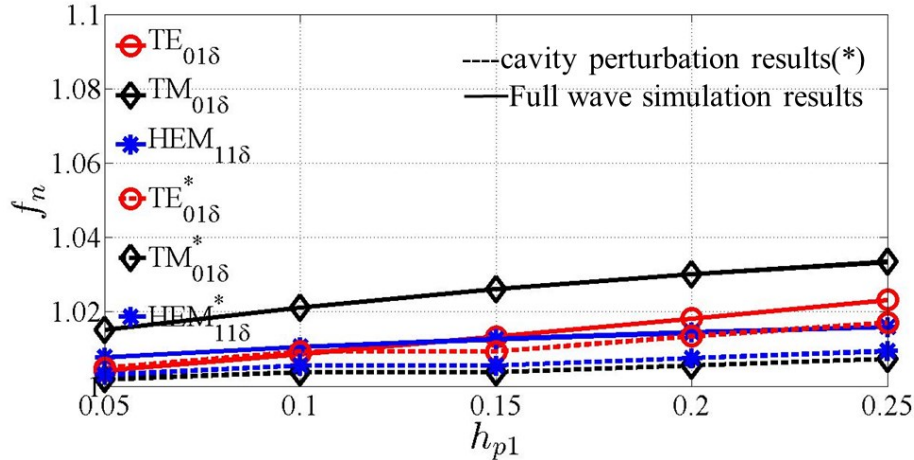
Fig. 3-15: Normalized frequency responses with a normalized bottom height of DR of ε_r=35 when Δr=0.1

Now, both the cavity perturbation equations and full wave solver are used to perturb bottom part of the DR to shift $HEM_{11\delta}$ mode up. Fig 3-16 presents the f_n of three modes with different heights while keeping Δr fixed at 0.3. It is clear that when h_{p1} is larger than 0.3 not only $HEM_{11\delta}$ but other two modes also start to shift up. Therefore, h_{p1} has to be maximum 0.3 or less.
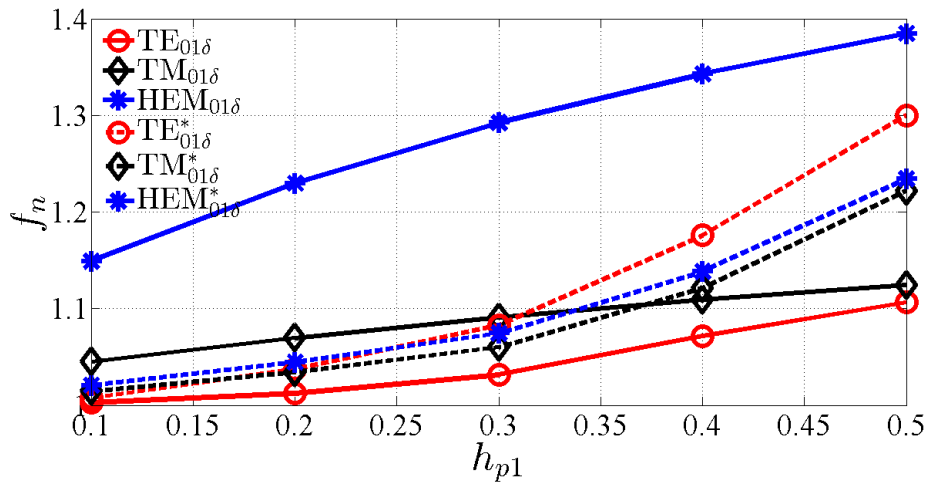
Fig. 3-16: Normalized frequency response of three modes with a normalized bottom cut height of DR of ε_r=10.2

Similarly, the cavity perturbation technique and full wave solver results are presented in Fig 3-17 for varying radius r_{p1} while fixing h_{p1} at maximum point 0.3. The radius of the perturbed area r_{p1} should be assigned cautiously so that $TM_{01\delta}$ mode does not get affected as it has a strong field at the center. On the other hand, variable r_{p1} cannot shift $TE_{01\delta}$ mode if h_{p1} does not reach

the strong field of this mode. It is visible when r_{pl} is 0.9 (Δr is 0.1) three modes reside at very close frequencies. It is also noticeable that when the radius is less than 0.5, other modes also shift. Hence r_{pl} has to be at least 0.5 or bigger to affect only $HEM_{11\delta}$ mode. Thus, the analysis presented in Fig. 3-16 and 3-17 provide the limits of perturbation parameters where h_{pl} has to be 0.3 or less, and r_{pl} has to be 0.5 or more.
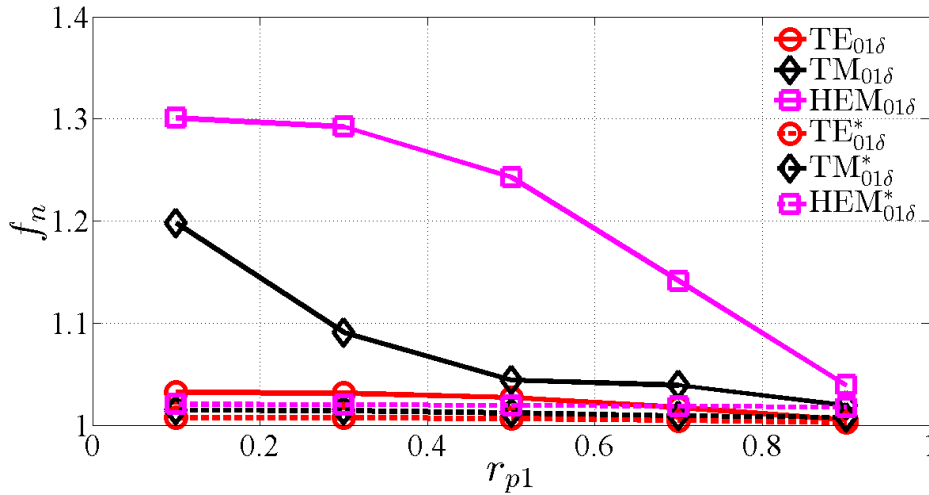
Fig. 3-17: Normalized frequency response of three modes with normalized perturbation radius of DR of ε_r=10.2

Using the limits, a tuning is applied to the perturbation parameters to obtain three modes at single frequency band. One of the possible solutions can be found when h_{p1}=0.2632 and r_{p1}=0.5639. Table 3-I presents both the unperturbed and perturbed DR response found from the Eigenmode solver where frequencies are normalized with f_1 (unperturbed TE mode frequency).

Table 3-I: Normalized frequency comparison of three modes in perturbed and unperturbed DR (normalized with unperturbed $TE_{01\delta}$ frequency)

Mode	f_N (unperturbed)	f_N (perturbed)
$TE_{01\delta}$	1	1.019
$HEM_{11\delta}$	0.92	1.018
$TM_{01\delta}$	0.954	0.962

From table 3-I, it can be noticed, after perturbing the bottom area, the three modes are located very close to each other, especially, $HEM_{11\delta}$ and $TE_{01\delta}$ can be found at the same

frequency. Therefore, the existing configuration of the DR is considered to excite them. Excitation techniques of the three modes are explained in the design section. It was found that the coupling to the $TE_{01\delta}$ mode is not possible using a planar structure as employed in [10]. This is a consequence of the weak electric field intensity near the coupling area in comparison to the full-disk case shown in Fig. 3-18. So, an additional approach should be considered to improve matching capability as illustrated in the next section. Fig 3-19 and 3-20 presented the unperturbed and perturbed $HEM_{11\delta}$ and $TM_{01\delta}$ mode electric field and electric energy distributions.
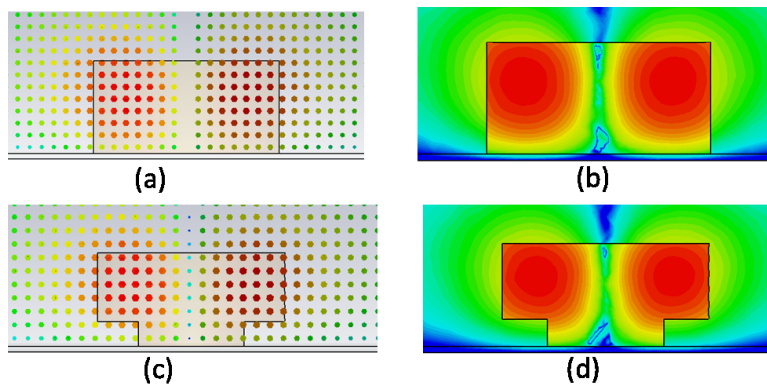
Fig. 3-18: The unperturbed $TE_{01\delta}$ mode (a) electric field (b) electric energy,
Perturbed $TE_{01\delta}$ mode (c) electric field (d) electric energy
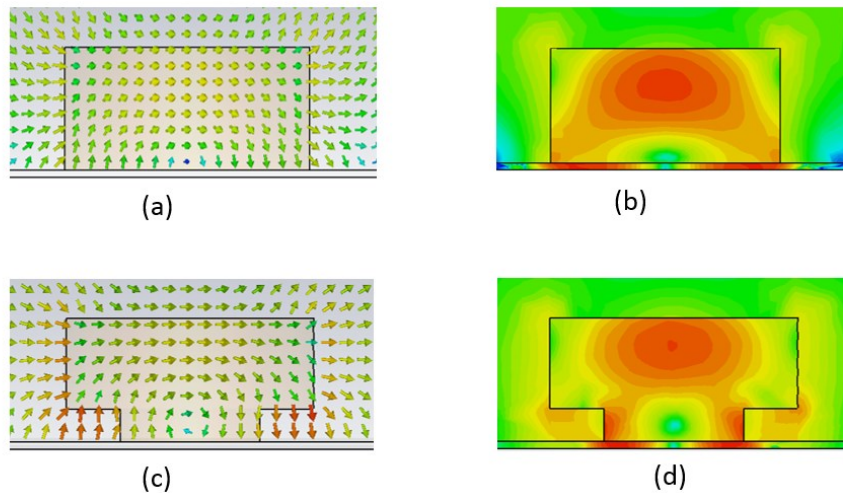
Fig. 3-19: The unperturbed $HEM_{11\delta}$ mode (a) electric field (b) electric energy,
Perturbed $HEM_{11\delta}$ mode (c) electric field (d) electric energy
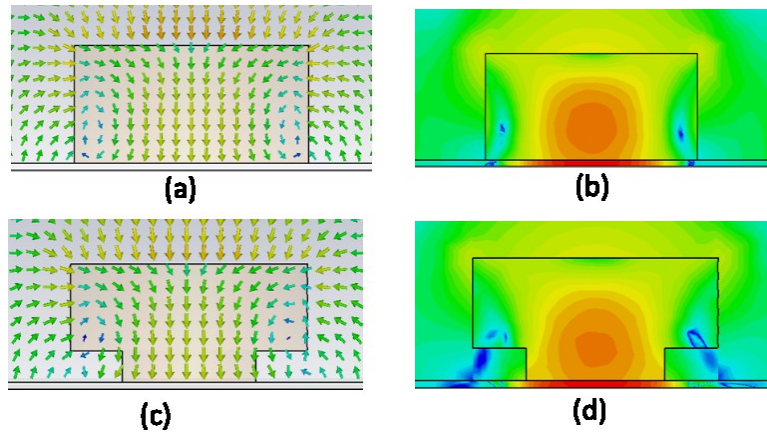
Fig. 3-20: The unperturbed $TM_{01\delta}$ mode (a) electric field (b) electric energy,
Perturbed $TM_{01\delta}$ mode (c) electric field (d) electric energy

3.3.2 Metal placement on top of the resonator to improve the matching of $TE_{01\delta}$ mode
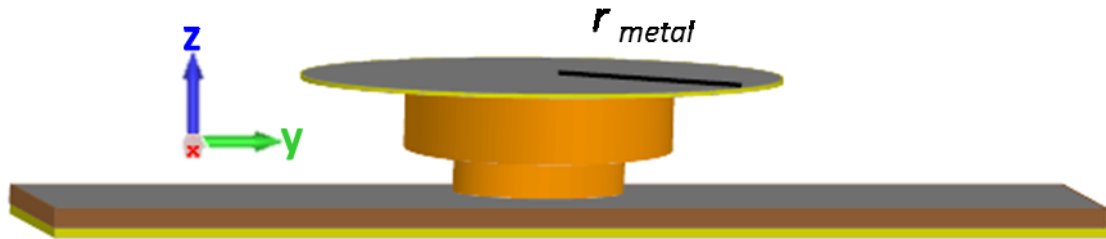
Fig. 3-21: DR with bottom part perturbation and a metallic cap on top

When a metal plate is placed on top of the resonator, the tangential electric field becomes zero at the metal boundary, and the electric energy of the DR near substrate becomes stronger. This helps to improve the matching capability of the $TE_{01\delta}$ mode with the microstrip line feeding network. In addition, the position of the metal on top can be varied by using foam that has the same permittivity as air. It was found that placing the metal directly on top of the resonator gives the best response in terms of impedance matching and insertion loss as a direct consequence of increasing the $TE_{01\delta}$ mode quality factor. Fig. 3-22 shows the effect of the metal on electric energy of $TE_{01\delta}$ mode compared to the energy without the metal.

<div align="center">(a)   (b)</div>
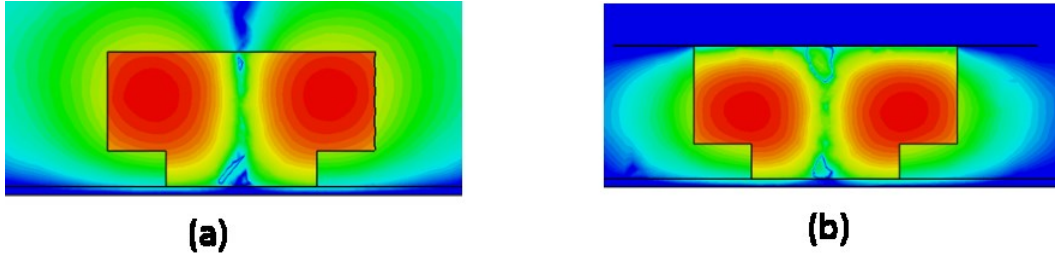
Fig. 3-22: Electric field of $TE_{01\delta}$ modes (a) without metal and (b) with metal.

It can be noticed, without metal, the electric energy is leaking outside the DR, and near the substrate, it is weak while placing metal confines the energy inside DR and near the substrate, it is not weak anymore. Therefore, the microstrip line placed on the substrate can couple to this mode. In addition, metal placement has some effect on the field distribution of $TE_{01\delta}$ mode. As the metal confines the field inside the resonator, the strong field located in the middle part of the resonator where it was evenly distributed throughout the resonator before placing the metal. Table 3-II shows the normalized frequencies of the modes with and without metal. These frequencies are normalized with respect to the unperturbed $TE_{01\delta}$ mode frequency f_1.

Table 3-II: Normalized frequency (with respect to unperturbed $TE_{01\delta}$) responses of three modes without and with metal in perturbed DR

Mode	f_N (unperturbed)	f_N (without metal)	f_N (with metal)
$TE_{01\delta}$	1	1.019	1.23
$HEM_{11\delta}$	0.92	1.018	1.246
$TM_{01\delta}$	0.954	0.962	0.86

However, placing the metal on top shifts the resonance frequency up of both $TE_{01\delta}$ and $HEM_{11\delta}$ modes whereas decreases the resonance frequency of $TM_{01\delta}$ mode. The mode is its electric field is transverse to the axis of symmetry at the top of the resonator, which becomes zero upon introducing the metal boundary. This further shifts the field towards the bottom part of the resonator, resulting in an increase of the resonant frequency as shown in Fig. 3-23.

(a)

(b)
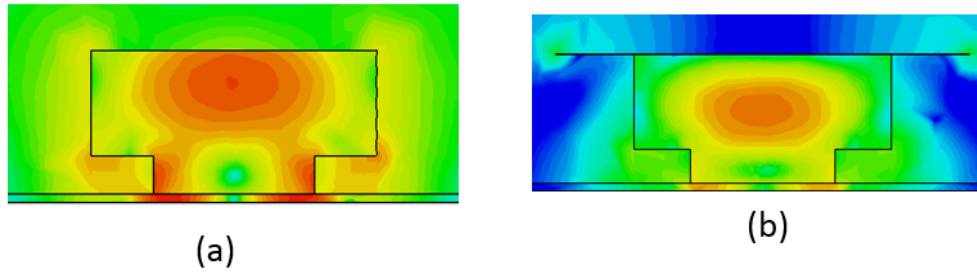
Fig. 3-23: Electric field distributions of $HEM_{11\delta}$ modes (a) without metal and (b) with metal.

The metal placement on top of the resonator solved the problem of $TE_{01\delta}$ mode excitation. $TM_{01\delta}$ mode has an orthogonal electric field to the resonator top wall that is loaded in a similar way as loading a monopole/dipole antenna, resulting in reducing the resonance frequency of this mode. As the $TM_{01\delta}$ mode that has been monitored till now shifted to a lower frequency, another $TM_{01\delta}$ mode has also been considered located closer to the frequency of interest. Fig. 3-24 presents electric energy distributions of these two modes in (b) and (c) in comparison with the $TM_{01\delta}$ mode without any metal.

(a)

(b)

(c)
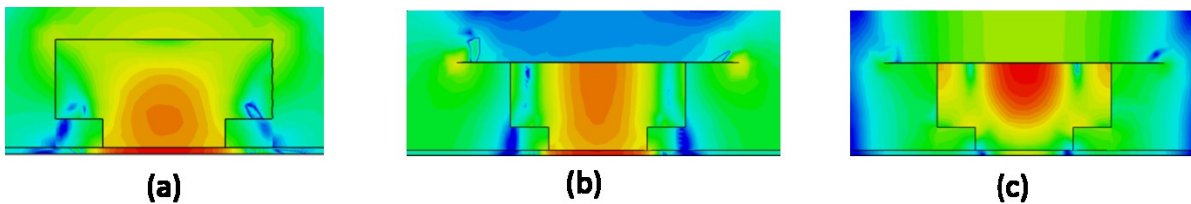
Fig. 3-24: Electric field distributions of $TM_{01\delta}$ modes (a) without metal (b) first $TM_{01\delta}$ mode with metal (c) second $TM_{01\delta}$ mode with metal

An excitation attempt was taken to couple to the new $TM_{01\delta}$ mode but was not successful. The analysis of the energy distribution of this mode shows an intense electric energy at the top part of the resonator because it sees the top metal as its ground plane. Thus, the probe cannot be coupled to it. Therefore, a decision is made to perturb top part of the resonator to modify the energy distribution of the second $TM_{01\delta}$ mode so that the probe can couple to it.

24

3.3.3 Perturbation of top part of the resonator
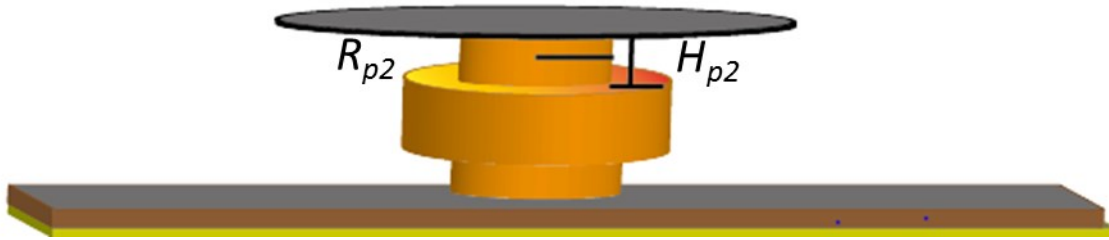
Fig. 3-25: DR with both top and bottom perturbation

As the electric field of the $TM_{01\delta}$ mode has both normal and radial components and for the second $TM_{01\delta}$ mode strong electric energy is located at the top part of DR. Hence a perturbation at the DR top part can tune this mode. In this case, the normalized perturbation height is h_{p2}, and the normalized perturbation radius is r_{p2} where the normalization is done with respect to the unperturbed DR height as it has been done for h_{p1} and r_{p1}. As the $TE_{01\delta}$ mode should be unchanged, therefore the height of the perturbation should be carefully chosen so that it does not affect the $TE_{01\delta}$ mode field distribution. The initial normalized height of the top perturbation h_{p2} is assigned to be same as h_{p1} that is 0.2632, and the responses of the modes with a different top part radius of DR are presented in Fig. 3-22. Here, mode frequencies are normalized with unperturbed $TE_{01\delta}$ frequency f_1 as it has been done before.
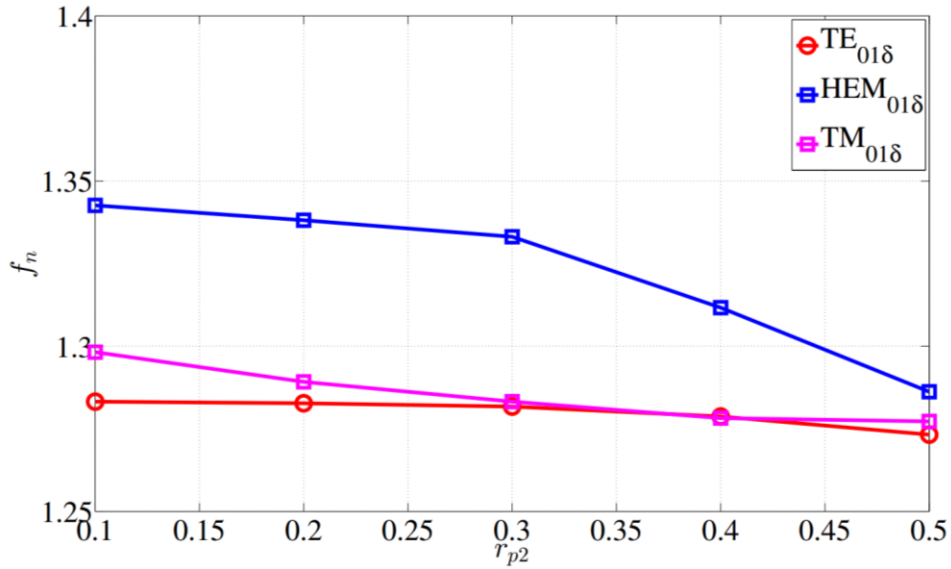
Fig. 3-26: Normalized frequency response of the modes with a normalized radius of the top perturbation

It is visible from Fig. 3-26 when r_{p2} is 0.4 to 0.5 these three modes reside very close to each other. Although this normalized frequency response gives an idea of the perturbation value, the energy distribution of the $TM_{01\delta}$ mode should be checked at the same time as it is not possible to couple to it unless the energy is located at the bottom part of the DR. The electric energy distribution of $TM_{01\delta}$ is displayed in Fig. 3-27. From Fig. 3-27 the electric energy of the $TM_{01\delta}$ mode is weak at the bottom part of the DR (a) that has been changed after the top perturbation (b) the top perturbation reduces some portion of the DR, thus forces the electric energy to shift towards the bottom area. Although reducing some portion of the top part is effective for $TM_{01\delta}$ mode, but it also shifts $HEM_{11\delta}$ mode frequency. On the other hand, it has shown in Fig. 3-26 when both normalized height h_{p1} and h_{p2} are 0.2632, the top perturbation does not affect $TE_{01\delta}$ mode. Therefore, by fixing normalized heights, it is possible to keep $TE_{01\delta}$ unchanged and then to tune r_{p1} and r_{p2} to bring $HEM_{11\delta}$ and $TM_{01\delta}$ at the same frequency as $TE_{01\delta}$. It is found that r_{p1}=0.5639 and r_{p2}=0.451 provide closest values of interested three modes that can be excited at the same frequency. Table 3-III shows the normalized frequencies of the modes after the top perturbation.
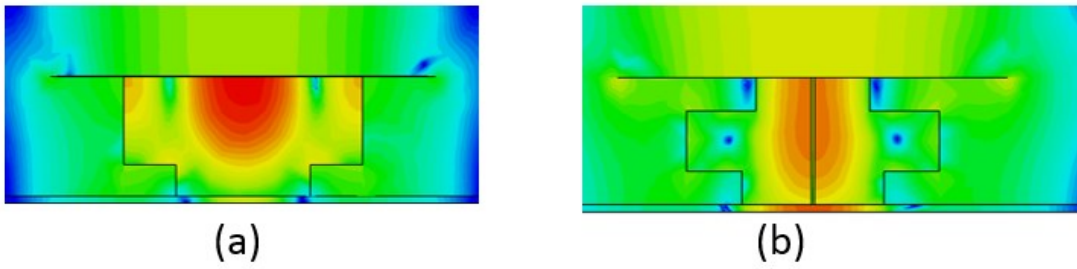
Fig. 3-27: Electric field distributions of $TM_{01\delta}$ modes, (a) before top perturbation and (b) after top perturbation

Table 3-III: Normalized frequency (with respect to unperturbed $TE_{01\delta}$) responses of three modes after top perturbation of DR

Mode	f_N (unperturbed)	f_N (without metal)	f_N (with metal)	f_N (top perturbation)
$TE_{01\delta}$	1	1.019	1.23	1.275
$HEM_{11\delta}$	0.92	1.018	1.246	1.3
$TM_{01\delta}(1)$	0.954	0.962	0.86	0.88
$TM_{01\delta}(2)$	-	-	1.22	1.285
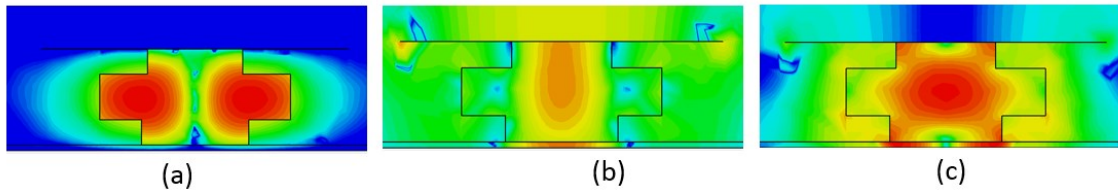
Fig. 3-28: Electric Energy distribution (a) $TE_{01\delta}$, (b) $TM_{01\delta}$ and (c) $HEM_{11\delta}$ modes after top perturbation.

The above-mentioned perturbation technique is applied on the DR of $\epsilon_r = 10.2$, but this method can be used in other dielectric constant materials also. To provide some general ideas on the shape perturbation, the following analysis has been considered.

3.4 Several approaches of DR geometry perturbation

In this section, a DR of $\epsilon_r = 35$ is also considered to explain some general techniques of perturbation. Several parts of the resonator are reduced to tune the modes.
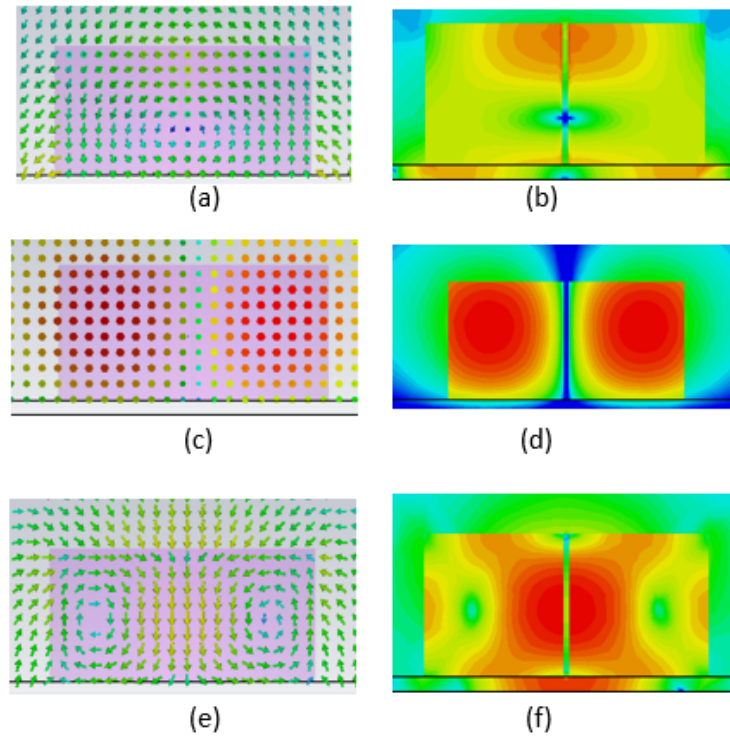
Fig. 3-29: Electric field and energy distributions of unperturbed DR of $\epsilon_r = 35$ (a) and (b) $HEM_{11\delta}$, (c) and (d) $TE_{01\delta}$; and (e) and (f) $TM_{01\delta}$ modes.

Fig. 3-29 shows the unperturbed dielectric resonator modes, electric fields, and energy distributions. The normalized values of $TM_{01\delta}$, $TE_{01\delta}$, and $HEM_{11\delta}$ modes are found to be 1.3, 1 and 0.994, respectively, and the normalization is done with respect to the unperturbed $TE_{01\delta}$ mode frequency. As it has been shown, placing a metal on the top is essential to excite the $TE_{01\delta}$ mode. Therefore, the analysis is done after the metal placement. Fig. 3-30 displays the electric

field and energy distributions of the modes where it is clearly visible that the energies of the modes are adequately confined inside the DR after placing the metal on top. The normalized value of the metal radius is kept same as the initial used value.
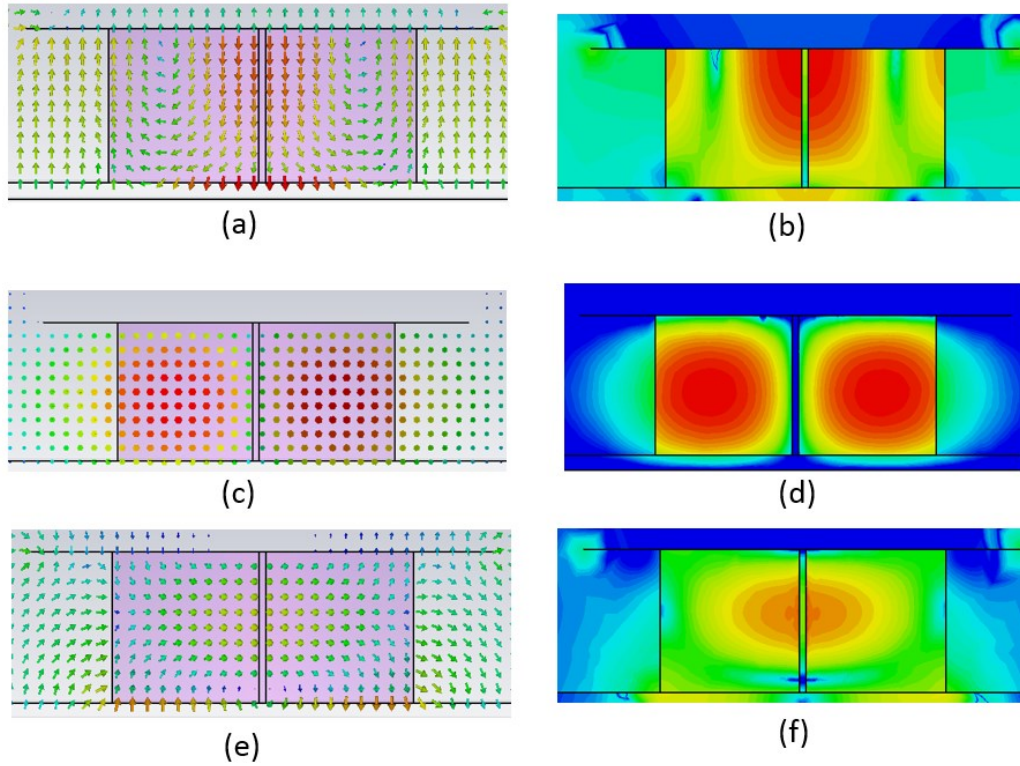
Fig. 3-30: The unperturbed DR of $\epsilon_r = 35$ with metal cap (a) electric field of $TM_{01\delta}$ mode, (b) electric energy of $TM_{01\delta}$ mode, (c) electric field of $TE_{01\delta}$ mode, (d) electric energy of $TE_{01\delta}$ mode and (e) electric field of $HEM_{11\delta}$ mode, (f) electric energy of the $HEM_{11\delta}$ mode

It is expected that placing metal on top will shift the resonance frequency of $TM_{01\delta}$ mode down and $HEM_{11\delta}$ and $TE_{01\delta}$ mode frequencies will go up. The normalized values of the $TM_{01\delta}$, $TE_{01\delta}$, and $HEM_{11\delta}$ modes are 1.11, 1.15 and 1.19 respectively. Fig. 3-30 shows the location of the strong electric field of $TM_{01\delta}$ mode at the top of the resonator that can be perturbed to shift the resonance frequency of this mode closer to $TE_{01\delta}$ mode. This simple perturbation of 32 provides TM ($f_n = 1.155$), and TE ($f_n = 1.155$) modes together.
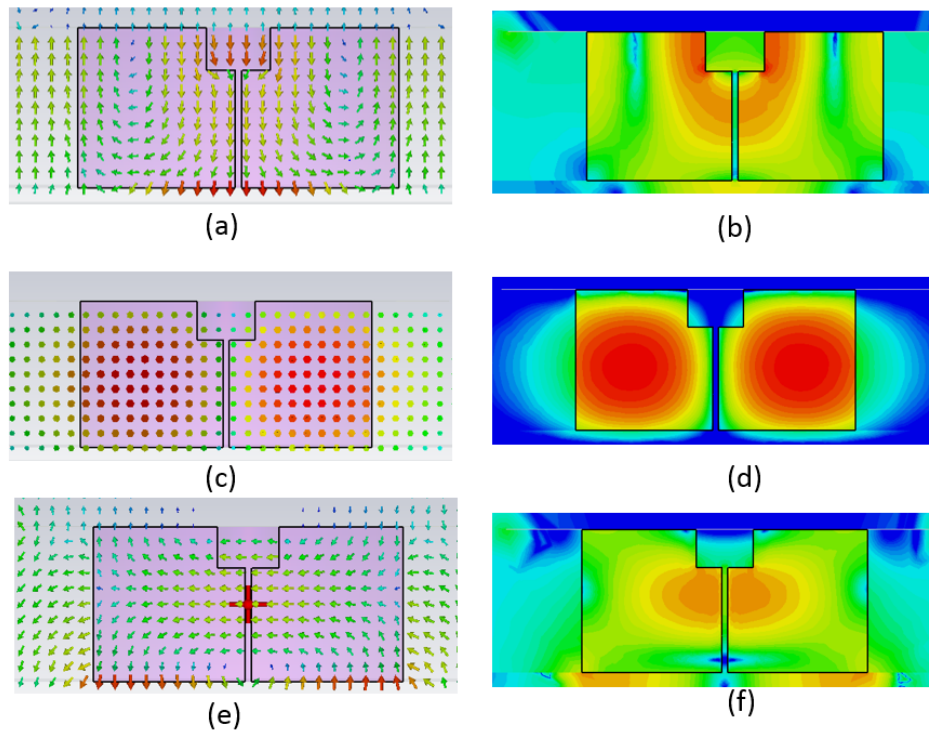
Fig. 3-31: Top perturbation of DR of $\epsilon_r = 35$ (a) electric field of $TM_{01\delta}$ mode, (b) electric energy of $TM_{01\delta}$ mode (c) electric field of $TE_{01\delta}$ mode (d) electric energy of $TE_{01\delta}$ mode (e) electric field of $HEM_{11\delta}$ modes,(f) electric energy of $HEM_{11\delta}$ modes

Fig. 3-31 presents the perturbation technique to obtain TE and TM modes together where Fig. 3-32 shows the tuning of $TE_{01\delta}$ mode along with other modes. The normalized values of $TM_{01\delta}$, $TE_{01\delta}$, and $HEM_{11\delta}$ modes are 1.259, 1.227, and 1.227, respectively. These values indicate that all $TE_{01\delta}$ and $HEM_{11\delta}$ modes have same resonance frequency where $TM_{01\delta}$ mode also has a very close value.
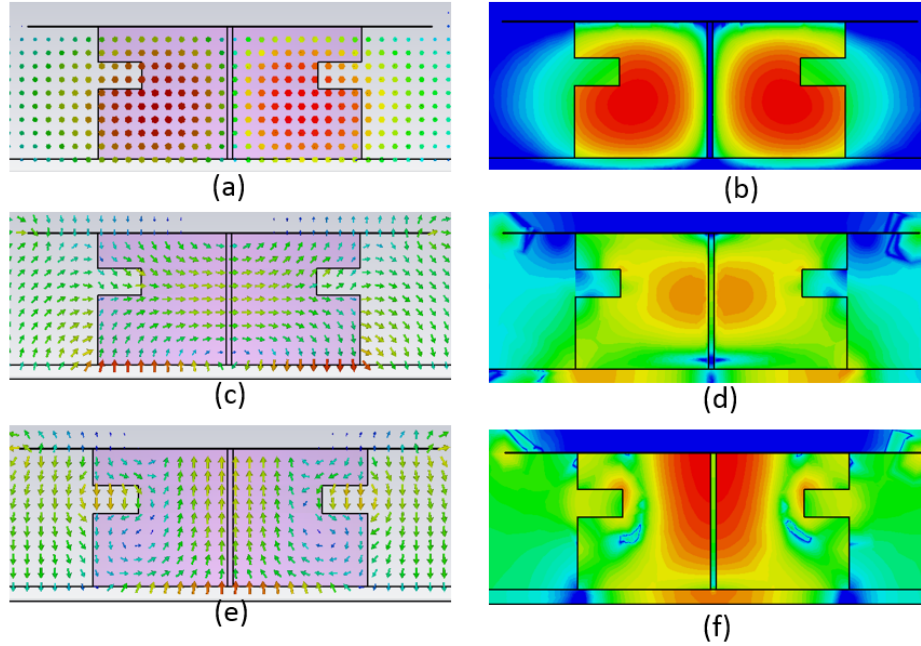
Fig. 3-32: Mid perturbation of DR ($\epsilon_r = 35$) (a) electric field of $TE_{01\delta}$ mode, (b) electric energy of $TE_{01\delta}$ mode (c) electric field of $HEM_{11\delta}$ mode (d) electric energy of $HM_{11\delta}$ mode (e) electric field of $TM_{01\delta}$ modes,(f) electric energy of $TM_{01\delta}$ modes

The concept of perturbing only the middle part of the DR of $\epsilon_r = 35$ is also applied to the DR of $\epsilon_r = 10.2$. The similar response is found from DR of ϵ_r 10.2 as 35, which is presented in Fig. 3-33. The energy distributions of $TM_{01\delta}$ mode show the strong energy is not only located on the top part but also it is strong at the bottom, which indicates it will be more accessible to couple to this mode with the probe. On the other hand, same, normalized perturbation values have been used here as it was used in perturbing middle part of the DR of $\epsilon_r = 35$, but normalized frequencies are not found to be same. The normalized frequencies of $TM_{01\delta}$, $TE_{01\delta,}$ and $HEM_{11\delta}$ modes are 1.215, 1.17 and 1.08 respectively. Thus, it needs to tune these parameters a bit to get closer resonance frequencies for all three modes.
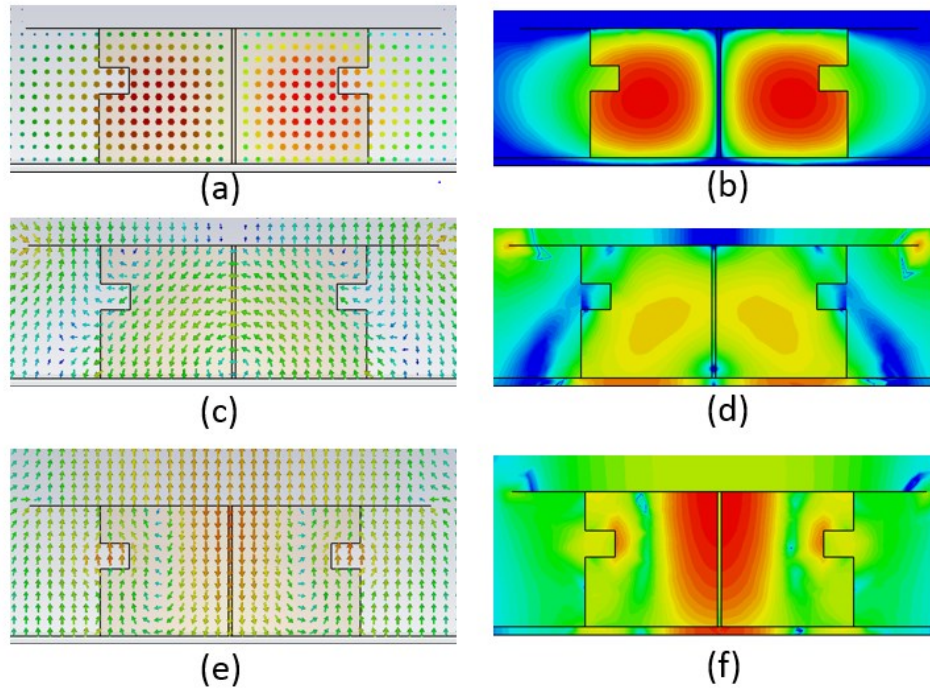
Fig. 3-33: Mid perturbation of DR (ϵ_r = 10.2) (a) electric field of $TE_{01\delta}$ mode, (b) electric energy of $TE_{01\delta}$ mode (c) electric field of $HEM_{11\delta}$ mode (d) electric energy of $HM_{11\delta}$ mode (e) electric field of $TM_{01\delta}$ modes,(f) electric energy of $TM_{01\delta}$ modes

To summarize, the perturbation of dielectric resonator has been done depending on the field distribution and energy distribution of the modes. From the above analysis, it is possible to tune the resonance frequency of one mode without much affecting the other modes.

Chapter 4

Geometry Perturbation of Dielectric Resonator for Multifunctional operation in WLAN frequency band

The dielectric resonator of permittivity ϵ_r =10.2 (Rogers 6010) is used considering the design cost and its availability. The structure is designed for Wi-Fi application that can work at 2.45 GHz. The dimensions mentioned in the previous analysis are used in the design. Because of its high Q factor, the lowest order mode $TE_{01\delta}$ is used for filter application where the $HEM_{11\delta}$ mode is excited to work as a broadside antenna, and $TM_{01\delta}$ is considered to operate as an omnidirectional antenna.

A two-layer substrate of Rogers 5880, $\epsilon_r = 2.2$, each of thickness 1.575 mm aligned back to back to design the feeding network for all modes where a ground plane is placed in between to separate them. The top substrate is allocated to fix the ports of $TE_{01\delta}$ mode and the bottom substrate is assigned to the ports of two antennas using $TM_{01\delta}$ and $HEM_{11\delta}$ modes. Among four ports- port 1, 2 excites $TE_{01\delta}$ and port 3, 4 are used to feed $TM_{01\delta}$ and $HEM_{11\delta}$ mode respectively. Fig. 4-1 displays the filter and antenna configuration with feeding mechanism.

Table 4-I: dimensions of DRA from early mentioned perturbation technique

Parametric Symbols	values	Parametric Symbols	values
h_{DR}	$0.57\lambda_g$	h_{p1}	0.2632
r_{DR}	$0.57\lambda_g$	h_{p2}	0.2632
r_{p1}	0.5639	l_{sub}, w_{sub}	$3.75h_{DR}$
r_{p2}	0.451	h_{sub}	1.575 (mm)
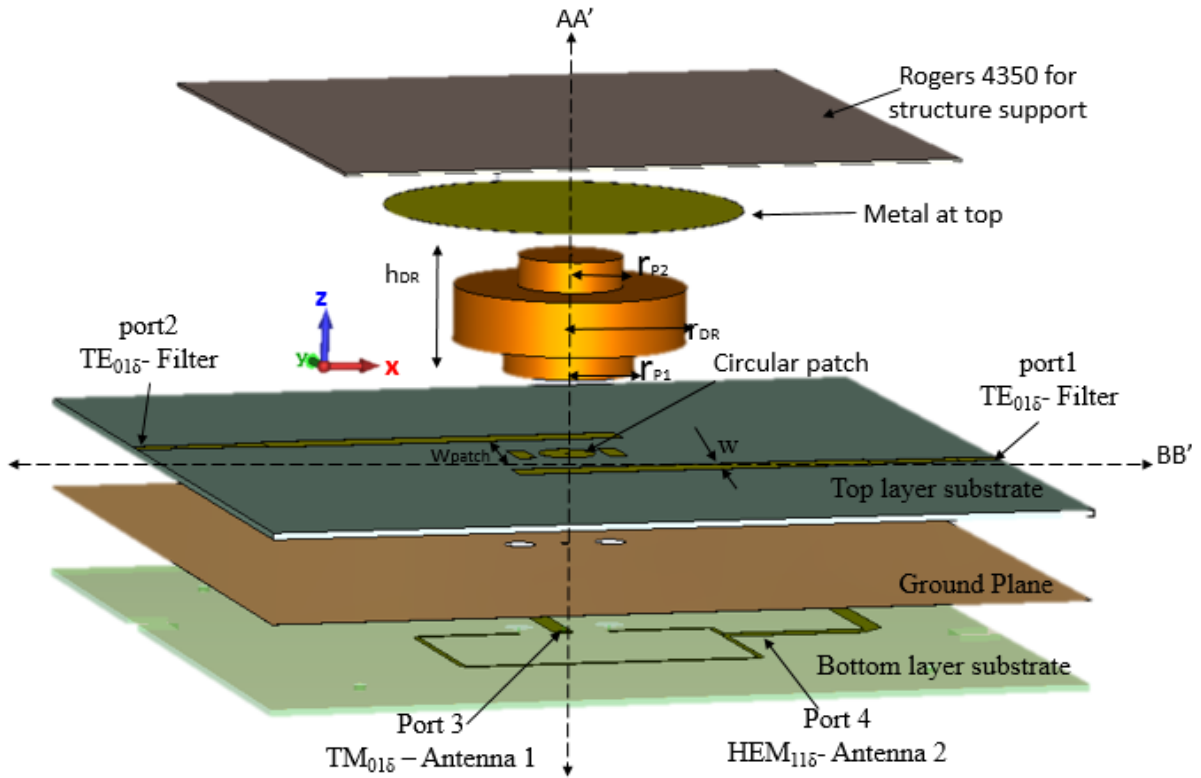
Fig. 4-1: Exploded view of the designed DRA

All the dimensions used in this design follow the perturbation technique that has been illustrated in the previous chapter and all implemented dimensions are listed in Table 4-II. The height of the DR is $h_{DR}= 0.57\lambda_g$ of unperturbed $TE_{01\delta}$ mode frequency which is 1.92 GHz here. As the aspect ratio is 1, thus the radius of the DR, R_{DR} is equal to the height H_{DR}. The used substrate parameters are length, l_{sub}, width and thickness, h_{sub}. The top and bottom perturbation normalized heights (h_{p1}, h_{p2}) and radius (r_{p1}, r_{p2}) are also kept same where all normalization is done with respect to h_{DR}.

Table 4-II: Dimensions of perturbed DRA design

Parameters	Dimensions (mm)
$w_{sub}=l_{sub}$	100
h_{sub}	1.575
r_{DR}	27.784
h_{DR}	27.784
r_{p1}	15.667
r_{p2}	12.534
$h_{p1}=h_{p2}$	7.3115

The design procedure is organized to explain three different excitation techniques for three modes. At first, the feeding mechanism of $TE_{01\delta}$ mode using microstrip line is mentioned. The second step describes the excitation technique through a 180° power divider, applied for a $HEM_{11\delta}$ mode that works as a broadside antenna. The third step defines the excitation of an omnidirectional antenna incorporating $TM_{01\delta}$ mode using a coaxial probe. Because the $TM_{01\delta}$ mode feeding needs to insert a wire, therefore an annular hole is created at the center of DR of diameter $d_{in} = 0.65mm$ same as the wire diameter.

4.1 Excitation of $TE_{01\delta}$ mode as a filter

Because of its high Q factor, the lowest order mode $TE_{01\delta}$ is most widely used for filter applications [21]. It can be easily coupled to the microstrip lines placed on the top layer of the substrate [48]. Matching between the microstrip line and DR is dependent on the following parameters: microstrip line width (*w*), distance between DR and line (*d*), metal radius (r_{metal}) and metal position. The dimensions of the parameters to excite $TE_{01\delta}$ mode are found through a parametric study of full wave solver, presented in table 4-III. It is found that for the microstrip line width *w,* impedance is 36Ω. To build a bandpass filter, two 36Ω microstrip lines are arranged at a distance of d= $\lambda_g/8$ from the edge of the bottom part of the resonator. Here straight microstrip lines are used to provide more space for the $HEM_{11\delta}$ mode feeding network. A quarter

wave microstrip line is added at $d_1 = 7*\lambda_g/4$ far away from the DR center to connect the line to a 50Ω port. The thickness of the substrate has to be large enough for the microstrip line to properly couple to the resonator.

As mentioned earlier, the metal on top of the resonator is a crucial factor to improve the impedance matching of the $TE_{01\delta}$ mode as it shields the DR to increase Q factor. To get a better matching of less than 15 dB a metal of radius $r_{metal} = 1.54R_{DR}$ is loaded at the top of DR. Increasing metal radius improves matching, but the limitation here is too big metal affects the $TM_{01\delta}$ mode as it has a radial component of electric field outside DR.

Table 4-III: $TE_{01\delta}$ excitation dimensions

Parameters	Dimensions(mm)
d	4.763
d_1	67.78
w	7.87
r_{metal}	42.825
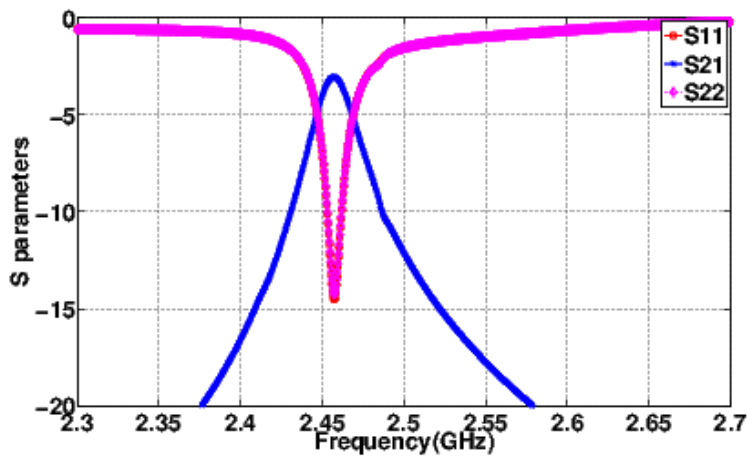
Fig. 4-2: Reflection and transmission coefficient of $TE_{01\delta}$ mode

36

To construct a bandpass filter at 2.45 GHz, two symmetric microstrip lines are placed on the top layer of the substrate. Although increasing metal dimension has a limitation, increasing metal radius can improve the transmission coefficient. Fig. 4-2 shows both ports reflection coefficient S_{11} and S_{22} to be around 15 dB whereas the transmission coefficient S_{21} is around 3 dB.

4.2 Excitation of HEM$_{11\delta}$ mode

As the electric field of the HEM$_{11\delta}$ mode is not axially symmetric, it needs a differential feeding mechanism. Therefore, a differential feeding power divider is designed to provide 180° phase shift at two sides of the resonator. To reduce the coupling and to give more space to each feeding system this power divider is fixed carefully on the BB' plane at the bottom layer of the substrate where TE$_{01\delta}$ feeding is located at the AA' plane of the top layer substrate as shown in Fig. 4-1. For the HEM$_{11\delta}$ mode, excitation is assigned at the bottom substrate, and it cannot be coupled to the resonator. Hence it is connected through vias to the patches underneath the resonator that couples to the DR.

4.2.1 Designing power divider that provides 180° phase shift

Two parallel 100Ω microstrip lines having the $\lambda_g/2$ distance in between are joined together to connect with a 50Ω port as shown in Fig. 4.1. The length of the power divider can be chosen randomly but should be a multiple of $\lambda_g/2$ to maintain the differential characteristics. Two ports are assigned to the 100Ω microstrip lines to measure the transmission from 50Ω port. Fig. 4.3 shows the phase variation of two microstrip lines where 180° phase difference is noticeable at 2.45 GHz. It is important to note that to avoid discontinuity problems, each microstrip line junctions are bent, so there is no loss of power. There are some additional bends in the power divider to provide more space for the TM$_{01\delta}$ mode feeding system.
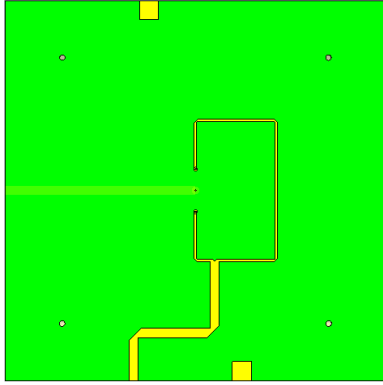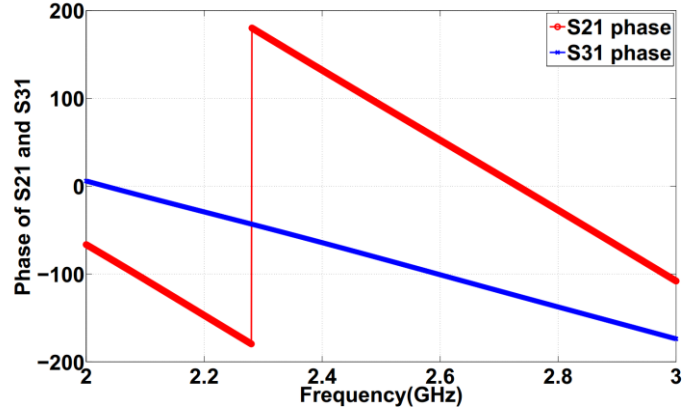
(a)	(b)

Fig. 4.3: power divider to excite HEM$_{11\delta}$ mode (a) top view (b) phase variation of S parameters

4.2.2 Designing patches to couple to the DR

As the power divider is located at the bottom layer of the substrate and the resonator is placed on the top layer of the substrate, so the microstrip lines are not interacting with the DR. Therefore, two rectangular patches are placed at the top layer underneath the resonator that is connected to the power divider through conducting vias. To match the microstrip line with the resonator, three optimization parameters are critical which are as follows: the distance between patches and resonator d_{patch}, patch length l_{patch} and patch width w_{patch}. From the field distribution of HEM$_{11\delta}$ mode, it is visible that the orthogonal electric field components are located at the bottom edge, so the patch should be placed close to the edges of the resonator.

The designed patches are connected to the power divider through conducting vias. To make the connection lossless, a 100Ω microstrip line to 100Ω coaxial connection has been developed incorporating a circular patch at the tip of the 100Ω microstrip line. Here, the radius of the small circular patch, $r_{transition}$ is the parameter that can control transmission quality.

4.2.3 Increasing matching bandwidth using Slot on top of metal
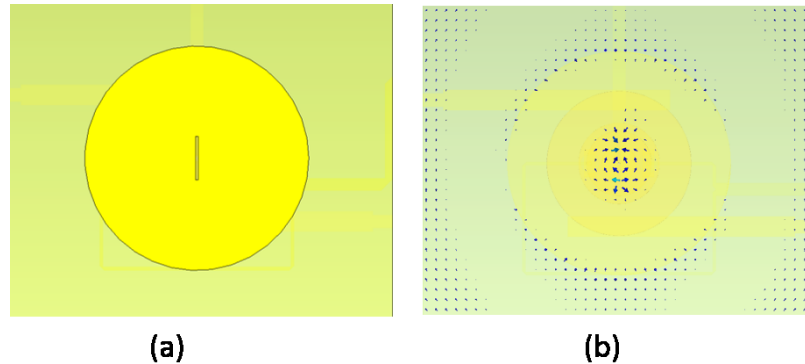
Fig. 4-4: HEM$_{11\delta}$ mode excitation (a) slot in the metal (b) magnetic field distribution of HEM$_{11\delta}$ mode on the metal

Although the impedance matching of the excited HEM$_{11\delta}$ mode is found to be better than 15 dB, the bandwidth is very narrow, which is not suitable for an antenna. The narrow bandwidth is because of the metal placed on top which increases the Q factor of this mode. Therefore, the additional approach is needed to improve the bandwidth, and a solution could be making a slot in the metal. The slot helps to decrease the radiating Q factor of the HEM$_{11\delta}$ mode and thus improving the bandwidth. The length, width, and position of the slot should be carefully chosen so that it does not affect other modes. As the slot cooperates with the magnetic field distribution, therefore it should be located parallel to the magnetic field of the HEM$_{11\delta}$ mode. Fig. 4-4 exhibits the slot position and the magnetic field distribution on the top metal that indicates the same alignment of the slot as the H field.

Fig. 4-5: Reflection coefficient of HEM$_{11\delta}$ mode excitation and TE$_{01\delta}$
with the coupling coefficient between them

Fig. 4-5 displays the reflection coefficient of HEM$_{11\delta}$ mode with the existence of TE$_{01\delta}$ mode feeding network. The HEM$_{11\delta}$ mode has excellent performance in terms of reflection coefficient that is less than 30 dB at 2.45 GHz. As both the rectangular patches that excite HEM$_{11\delta}$ mode and the transmission lines exciting TE$_{01\delta}$ mode located at the same layer of the substrate and very close to each other, hence it is expected to have a considerable coupling between them. However, at the operating filter point, there is a considerable coupling of around 15 dB. The 10 dB impedance matching the bandwidth of HEM$_{11\delta}$ mode operated broadside antenna is about 2% where it had a lower value without the slot on metal, and it covers the filter operating range. Table 4-IV presents the used dimensions to excite the HEM$_{11\delta}$ mode as an antenna element.

Table 4-IV: HEM$_{11\delta}$ mode excitation dimensions

Parameters	Dimensions (mm)	Parameters	Dimensions (mm)
d_{patch}	11.23	l_{patch}	4.433
w_{patch}	10.835	$r_{transition}$	1
l_{slot}	16.5	w_{slot}	1.018

4.3 Excitation of TM

The electric field distribution of $TM_{01\delta}$ is similar to an electric monopole. Therefore, it can be excited with a coaxial probe. As this mode is symmetric, the probe has to be inserted from the center of the DR, and this is why the inner diameter of the DR is kept equal to the probe wire diameter (0.64mm). The length of the inner conductor h_{probe} is the parameter to tune the resonance frequency of the $TM_{01\delta}$ mode and should be carefully selected to resonate at 2.45 GHz.

As there are several $TM_{01\delta}$ modes, it's difficult to excite the mode of interest with an acceptable impedance matching level because the intense electric energy is located at the top of the DR. To improve the matching a circular patch is placed underneath the resonator. As the electric field of this mode is orthogonal, using the patch does not affect the field, but, it improves the coupling between the $TM_{01\delta}$ mode and the probe. The combination of length h_{probe} of the probe and radius of the circular patch r_{patch} are the critical parameters to tune the coupling to $TM_{01\delta}$ mode.
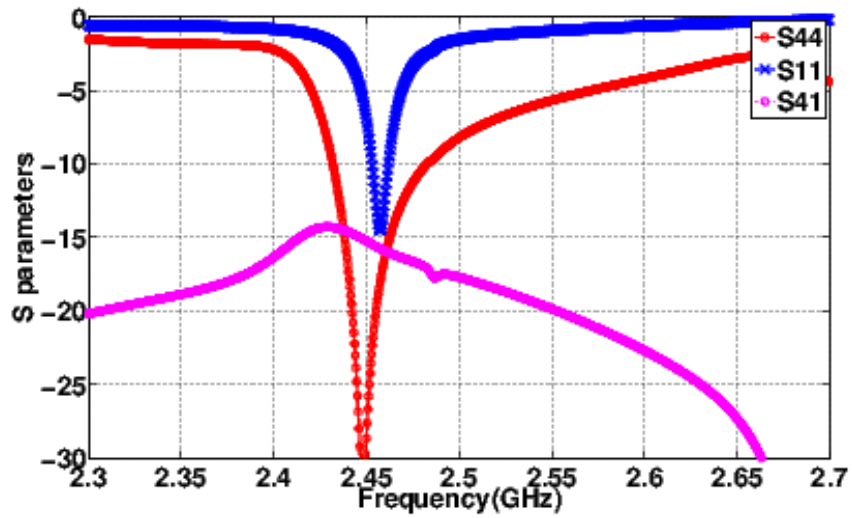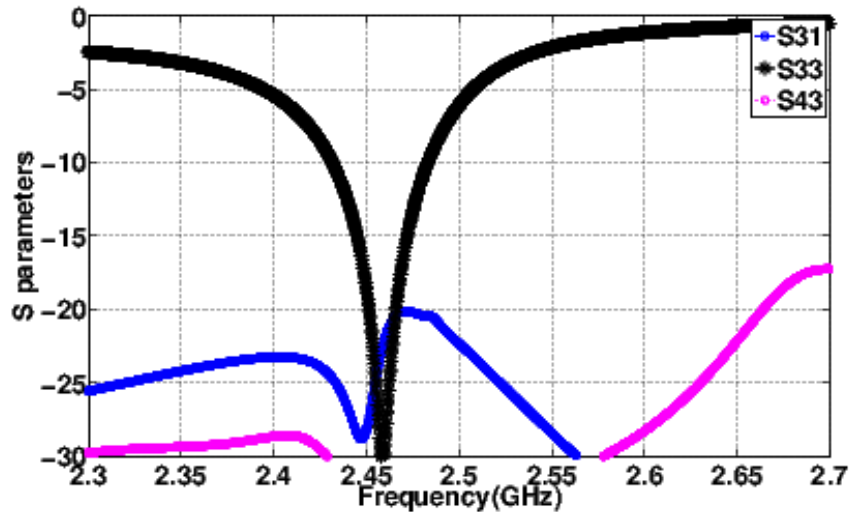

Fig. 4-6: Reflection coefficient of $TM_{01\delta}$ mode excitation and $TE_{01\delta}$ with the coupling coefficient between them

Fig. 4-6 illustrates the S parameters of $TM_{01\delta}$ mode. The port return loss is better than 30 dB at 2.45 GHz. Also, the coupling coefficients with $TE_{01\delta}$ mode S_{31} is less than 20 dB, and with the $HEM_{11\delta}$ mode, S_{43} is less than 30 dB that indicates its uninterrupted performance as an omnidirectional antenna.

4.4 Simulated and measured results

The proposed structure is verified using the full-wave simulations of CST (frequency domain solver) targeting the Wi-Fi operating frequency band centered at 2.45 GHz. The structure is then fabricated to investigate the practical scenario of the proposed perturbation method. Fig. 4-7 (a) shows the fabricated structure which is a combination of several small disks of DR which are added with glue. Fig. 4-7(b) displays the measured S parameters of three ports where frequency shift is noticeable among the ports.

(a)   (b)
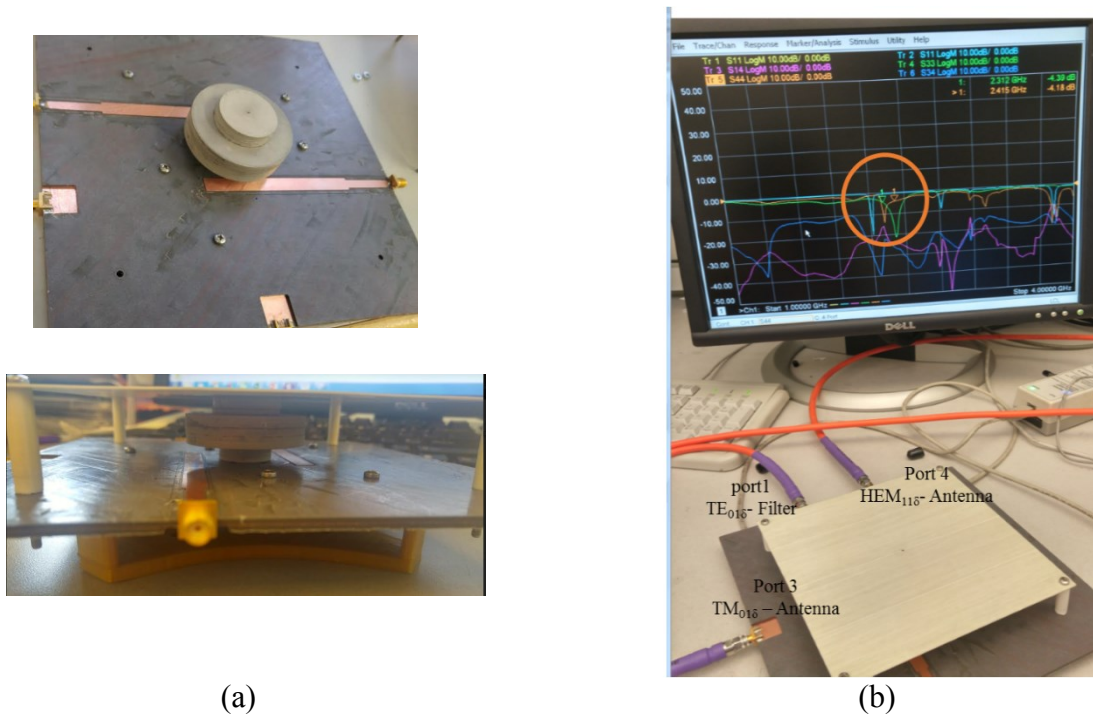
Fig. 4-7: (a) Fabricated prototype of DRA (b) measured S parameters

Fig 4-8 to 4-10 shows the comparison between simulated and measured results of $TE_{01\delta}$, $TM_{01\delta}$ and $HEM_{11\delta}$ modes respectively. For the measured $TE_{01\delta}$ mode a considerable frequency

shift is visible. The simulated one works at 2.45GHz where the measured one works at 2.23GHz. These frequency shifts are due to the combination of seven small disks forming the DR, which are connected with hot glue. This incorporated some gaps in between the disks as well as increasing the overall DR size, which is a critical factor in the observed frequency shift. Also, the $TE_{01\delta}$ mode is susceptible to the radius of the DR (R_{DR}) as its frequency shifts with varying aspect ratio. It is also possible that some misalignment exists between the pieces of resonators which causes this frequency shift. However, filter insertion loss improved in the fabricated structure. In fig. 4-8 simulated insertion loss is about 3dB which is 1.41dB at the measurement.
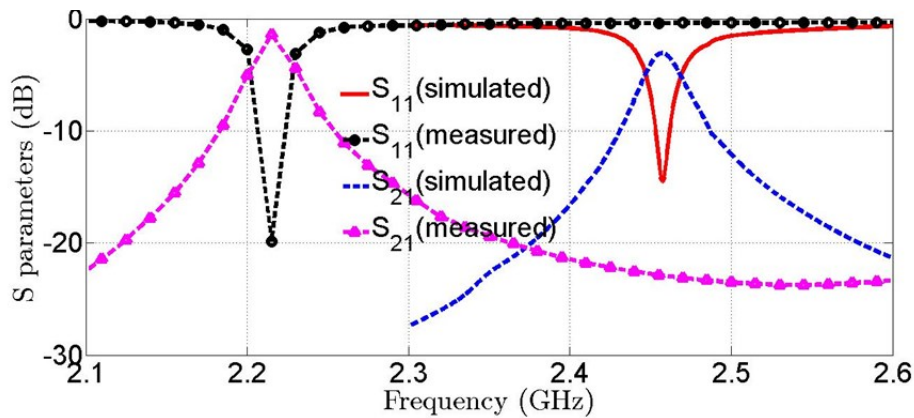
Fig. 4-8: Reflection, transmission coefficients of the proposed filter element of $TE_{01\delta}$ mode
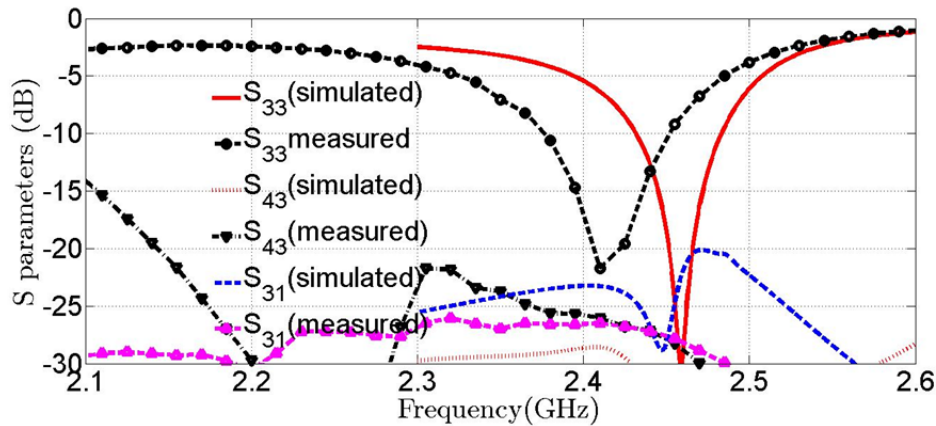
Fig. 4-9: Reflection and Coupling coefficients of the omnidirectional antenna element of $TM_{01\delta}$ mode
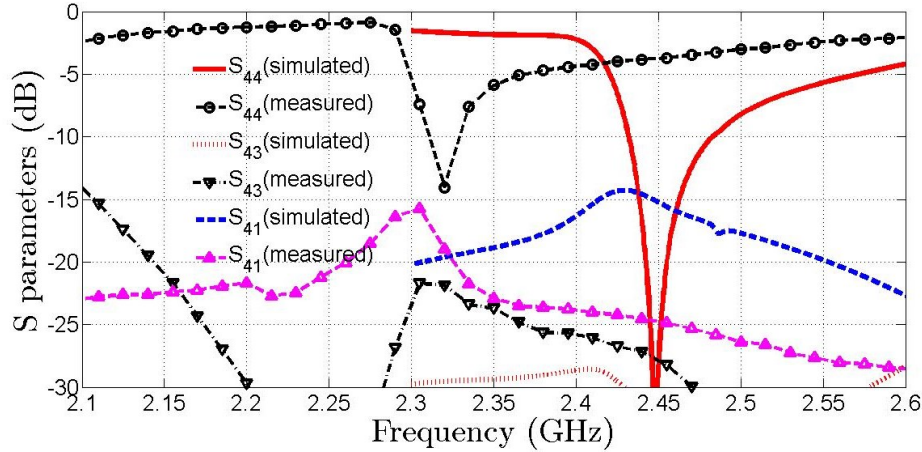
Fig. 4-10: Reflection and Coupling coefficients of the broadside antenna element of HEM$_{11\delta}$ mode

Fig. 4-9 and 4-10 present the reflection and coupling coefficients of the antenna ports. The simulated reflection coefficient of the TM$_{01\delta}$ mode is better than 30 dB at 2.45 GHz with 52 MHz impedance matching bandwidth, and its coupling with the other two modes are lower than -20 dB. The measured impedance matching bandwidth is 75 MHz, and the reflection coefficient is less than 20 dB at 2.41 GHz. Coupling between filter ports and Port 3 is less than 20 dB throughout the range which follows the simulation result. Similarly, the coupling between two antenna elements is less than 25 dB both in simulated and measured plots. The Simulated HEM$_{11\delta}$ mode results show the reflection coefficient below -30 dB at 2.45GHz but have a high coupling with TE$_{01\delta}$. This high coupling is due to the tightly located transmission lines of the TE$_{01\delta}$ mode excitation and the rectangular patches of HEM$_{11\delta}$ mode excitation. On the contrary, the measured HEM$_{11\delta}$ mode results in Fig.4-10 show a frequency shift of 130 MHz and about 15 dB port reflection. The reason for the frequency shift might be similar to causes of TE$_{01\delta}$ mode frequency shift.

Furthermore, it can be seen from the simulation results that the TE$_{01\delta}$ mode is covered by both the HEM$_{11\delta}$ and TM$_{01\delta}$ modes and the 10dB impedance matching bandwidth for both TM$_{01\delta}$ and the HEM$_{01\delta}$ mode are within the frequency range of 2.43-2.48 GHz. In contrast, the fabricated structure supports three modes in the same way but with frequency shifts.

To complete the performance check, the radiation patterns of the antennas are also measured. Fig. 4-11 shows the comparison between simulated and measured radiation patterns of HEM$_{11\delta}$

mode. Measured and Simulated E-Plane and H-Plane pattern show good agreement. As the simulated $HEM_{11\delta}$ mode worked at 2.45 GHz and measured antenna operates at 2.32 GHz, therefore radiation patterns at both frequencies are presented. The simulated gain and radiation efficiency of the broadside pattern antennas are found to be 5.37dB and 92% respectively.

(a)   (b)
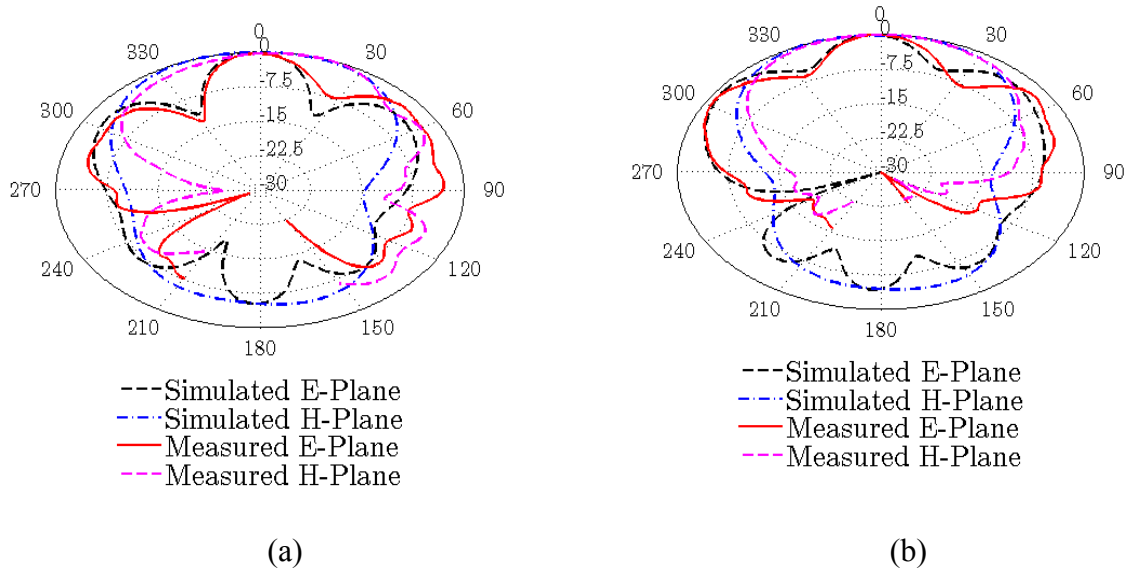
Fig. 4-11: Simulated and measured radiation pattern of $HEM_{11\delta}$ mode (a) 2.32 GHz. (a) 2.45 GHz.

Fig.4-12 represents the radiation pattern of the $TM_{01\delta}$ mode that has an omnidirectional pattern with a null at $\theta = 0$. The XZ and YZ plane radiation patterns of $TM_{01\delta}$ mode are shown in both simulated and measured design. Although a small variation has been found in the measured YZ plane, the pattern has the similar behavior as the omnidirectional antenna. Radiation patterns are provided for two frequencies as the simulated antenna works at 2.45 GHz, and the measured antenna shifted to 2.41 GHz. It is visible that the omnidirectional pattern is achievable at both frequencies. The gain and efficiencies of this antenna are 3.09dB and 94% respectively. This indicates that DRAs have low dissipation losses.

           (a)   (b)
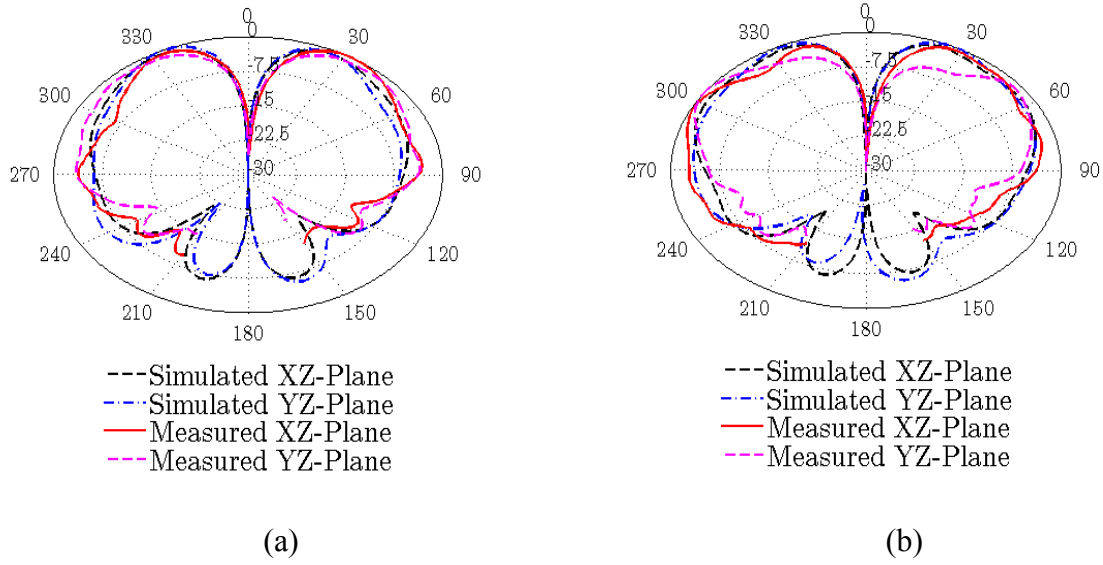
Fig. 4-12: Simulated and measured radiation pattern of $TM_{01\delta}$ mode (a) 2.41 GHz (b) 2.45 GHz.

As the concept of this design is to build a multifunctional MIMO device, it is essential to maintain the polarization and pattern diversities among the antennas. From the field distributions of $TM_{01\delta}$ and $HEM_{11\delta}$ modes, the orthogonal polarizations of these modes are clearly visible. Fig. 19 and 20 present orthogonal radiation patterns of the two antennas- omnidirectional $TM_{01\delta}$ pattern and broadside $HEM_{11\delta}$ pattern. To confirm MIMO antenna diversity performance, the envelope correlation coefficient between the two antennas of port 3 and 4 is calculated from S parameters [50]. The envelope correlation coefficient calculated using following equation:

$$\rho_e = \frac{|S_{33}^* S_{34} + S_{43}^* S_{44}|^2}{(1 - (|S_{33}|^2 + |S_{43}|^2))(1 - (|S_{44}|^2 + |S_{34}|^2))}$$

To calculate the ρ_e, imported S parameters from the full wave solver are used in the above equation. This equation can be used when the radiation efficiency is very high. As it is already found that both the antennas have high radiation efficiency, therefore the calculated correlation coefficient is accurate. Fig. 4-13 shows the envelope correlation coefficient is minimal within the frequency band of interest. Both the measured and simulated envelope correlation coefficients

46

are presented which indicates a good agreement among these and it has been found that the measured antenna diversity is better than the simulated one.
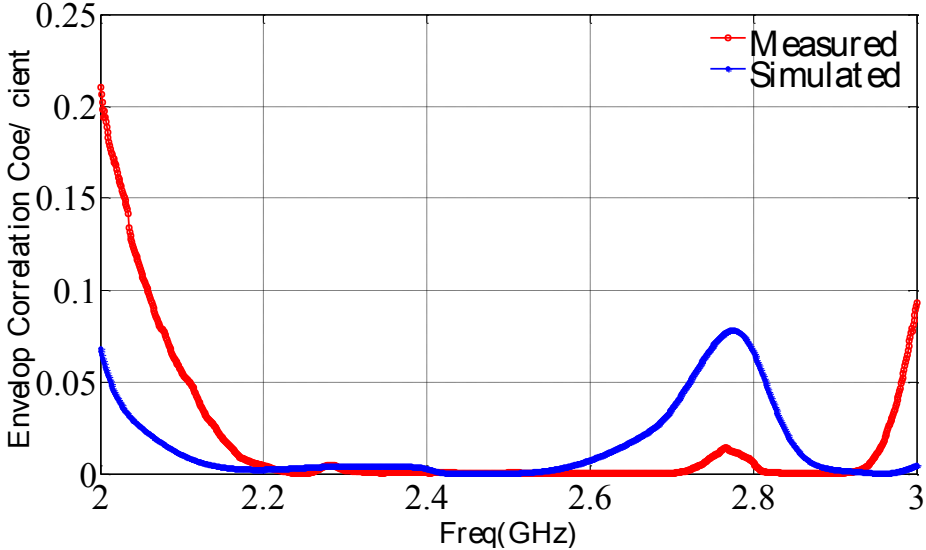
Fig. 4-13: Simulated and measured envelope correlation coefficient between two antennas calculated from S parameters

Chapter 5
Cascading two elements

The proposed single element device can be implemented in a two-element network where four antennas will work simultaneously with a second-order bandpass filter. This device will be a perfect candidate for MIMO application as the IEEE standard 802.11n states that a MIMO system requires minimum four antennas to operate individually [6]. After cascading two single elements, two of the antennas will radiate with an omnidirectional pattern having a null at the center, which will be covered by other two antennas with their broadside patterns. In addition, the filter co-operated by the $TE_{01\delta}$ modes in the single DR device can be incorporated here as a second-order bandpass filter. Thus cascading two elements support the concept of having both multi-functional devices as well as MIMO antennas.

To operate the $HEM_{11\delta}$ modes independently, the second element is orthogonally placed next to the first element. The filter elements are decided to be placed before assigning the antenna ports so that its performance can be monitored without external effects.

5.1 Adjustment of filter elements

The $TE_{01\delta}$ mode excitation lines are aligned in the similar way as it was before for the single element. Initially, when the filter ports are simulated keeping a minimum required distance ($d_{elements}$) in between, the insertion loss was found to be much lower than 10dB which is not considered as a filter. Therefore, a coupling network is designed between the two resonators which can transfer energies among $TE_{01\delta}$ modes. The parameters to design a better coupling network are the distance between the resonator and the coupling line ($d_{coupling}$), the width of the line ($w_{coupling}$) and the total length of the coupling line ($l_{coupling}$). Two different configurations are considered for cascading the resonators; one is placing them orthogonally to each other, and the other one is without any rotation as both structures have some advantages.

5.1.1 Orthogonal DRs with *L*-shape coupling network

An L-shape coupling network is designed between two dielectric resonators so that $TE_{01\delta}$ modes can transfer energies among two resonators. The selection of L shape came from the idea of maintaining symmetry between the coupling networks of $TE_{01\delta}$ modes as much as possible because this mode requires axial symmetry from its characteristics. Although the $TE_{01\delta}$ modes and the microstrip lines to excite these modes are symmetric, but a small asymmetry between the two ports of the $TE_{01\delta}$ mode is expected because of the orthogonal alignments of the slots in top shields of the resonators. It is noteworthy that it is not possible to make $l_{coupling}$ less than $1\lambda_{eff}$ (93mm) as the resonators overlap with each other. Therefore, multiples of $\lambda_{eff}/2$ and λ_{eff} are tested as $l_{coupling}$ to find an optimum filter response.
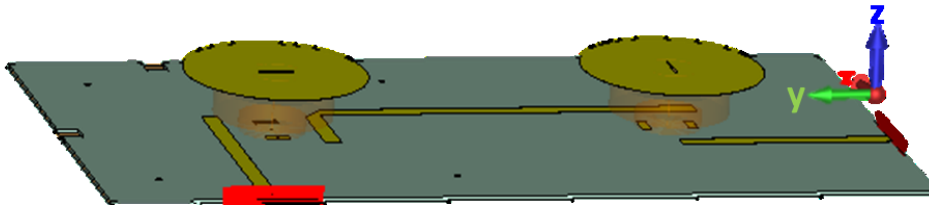
Fig 5-1: L shape coupling network between two DR

Another important note is, for the single element the return loss from the simulation was about 3 dB, although in measurement it improved to 1.41dB. Therefore, it is expected to get maximum 6dB or lower insertion loss from the simulation of the cascaded two elements. Keeping this in mind, research has been done to observe the best possible filter response by implementing a coupling network between two dielectric resonators. Fig. 5-2 presents the return loss and insertion loss found from filter ports when the *L* shape coupling line length ($l_{coupling}$) is 3 λ_{eff}, as it showed better responses compared to the other multiples. It has the highest insertion loss of about 6.5dB, which indicates that the total coupling length consumes only 0.5dB of transmitted power. However, the return loss for this length is around 8dB.
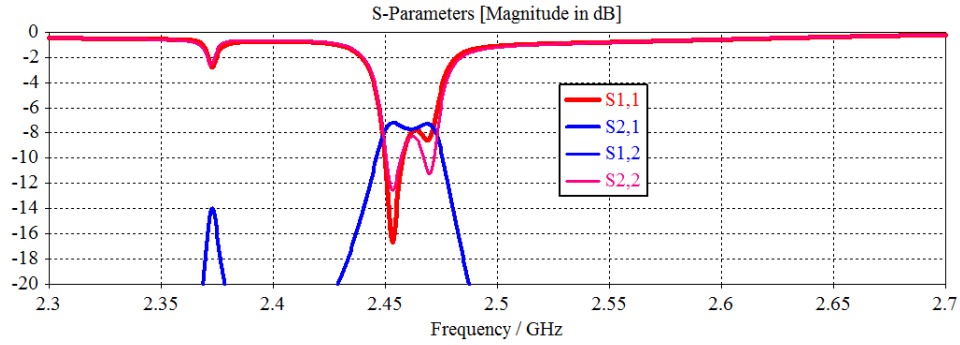
Fig 5-2: S parameters of filter ports with L shape coupling network (variable coupling length in terms of λ_{eff})

Table 5-I: Dimensions of parameters for optimum filter performance

Parameters	Value (mm)
$w_{coupling}$	7.87
$l_{coupling}$	231
$d_{coupling}$	4.76

5.1.2 Symmetric Alignment of two DRs with *S* shape coupling line

Another way to improve the $TE_{01\delta}$ modes symmetry is assigning a more extended coupling line in between the resonators which maintain more symmetry compared to the previous structure. However, the distance between the two resonators is small compared to the previous one. The second element is placed next to the first resonator without any rotation. Therefore the asymmetry because of the slots on top metals is avoided.
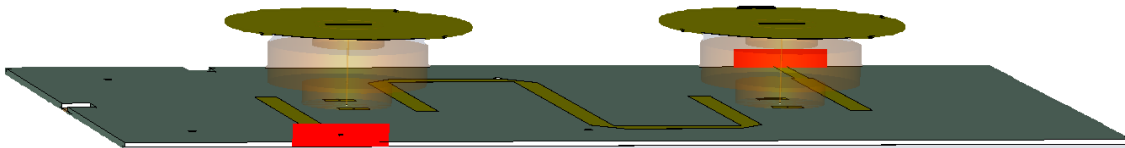
Fig 5-3: S shape coupling network between two DRs

Fig. 5-3 shows the S shape configuration of the coupling line between the resonators. The total length found for better coupling is $5* \lambda_{eff}$. As mentioned earlier, the structures are no longer orthogonal to each other. Therefore, the patches underneath and the slots on top of the resonator are oriented in the same direction. Fig 5-4 displays about 19dB impedance matching for both ports and 7.5dB insertion loss that specifies this more extended coupling line consumes about 1.5dB of the transmitted power. However, it is observed that matching becomes better when the coupling line length increases and thus the selected line length is a compensation for both matching and insertion losses.
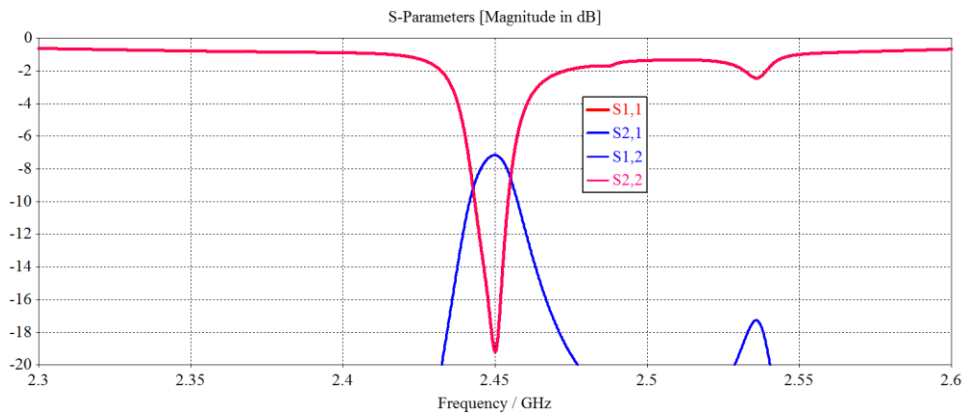
Fig 5-4: S parameters of filter ports with S shape coupling network

5.2 Assigning antenna ports

It is found that when the second element configuration is same as the first element with an S shape coupling line in between, can have better matching of the filter ports without any asymmetry. On the other hand, when the second element is orthogonal to the first one with an L shape coupling line, has a better insertion loss. Therefore, both of the structures are considered for the antenna design for multiple solutions.

5.2.1 Orthogonal alignments of two DRs

The alignment of the antenna ports is modified so that these ports do not overlap with each other. The feeding networks of these modes are designed orthogonally to each other including the patches underneath both DRs. However, the $TM_{01\delta}$ modes are excited through the wires from the center as before. Fig 5-5 shows the feeding networks of $HEM_{11\delta}$ and $TM_{01\delta}$ modes at the bottom substrate layers. Port 3, 5 are the ports representing $TM_{01\delta}$ modes of element 1 and 2 respectively, whereas port 4 and 6 are assigned for $HEM_{11\delta}$ modes.
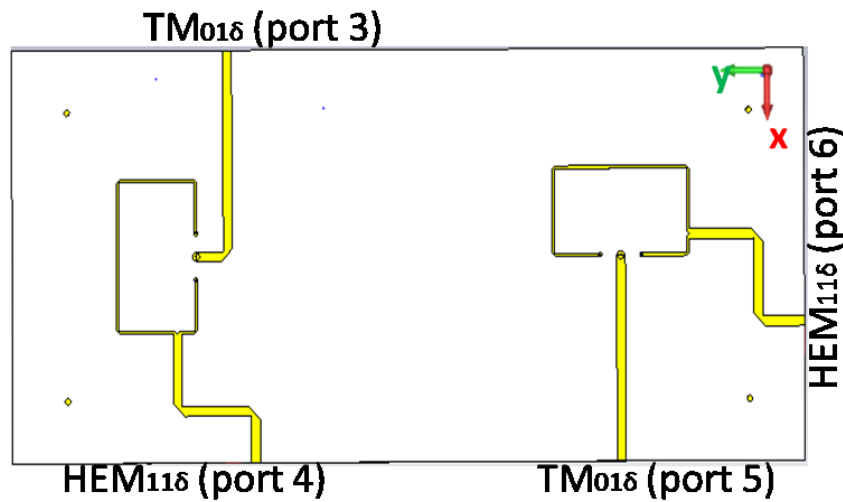
Fig. 5-5: Top view of the bottom substrate layer

The S parameters of the filter ports (1, 2) have some loading effects after fixing four antenna feeding networks. This loading effect is the result of the parasitic coupling between the filter parameters and antenna parameters. Although the impedance matching of port 1 and 2 was about 12dB without the presence of antennas, after assigning antenna ports these became around 8dB. On the other hand, the insertion loss is improved which is about 5.6dB with antenna ports is presented in Fig. 5-6.

Fig. 5-7 to 5-10 display the reflection and coupling coefficients of the four antenna ports. The 10dB impedance matching bandwidth of $TM_{01\delta}$ mode of the first element (port 3) is 2.62%

(64.48MHz). At resonance, reflection is less than 30dB and coupling with other antenna ports are less than 25dB that shows better performance of this antenna. However, with the filter ports, it has a coupling of about 18dB which might be the result of magnetic field coupling between $TM_{01\delta}$ mode and the coupling line between the resonators.
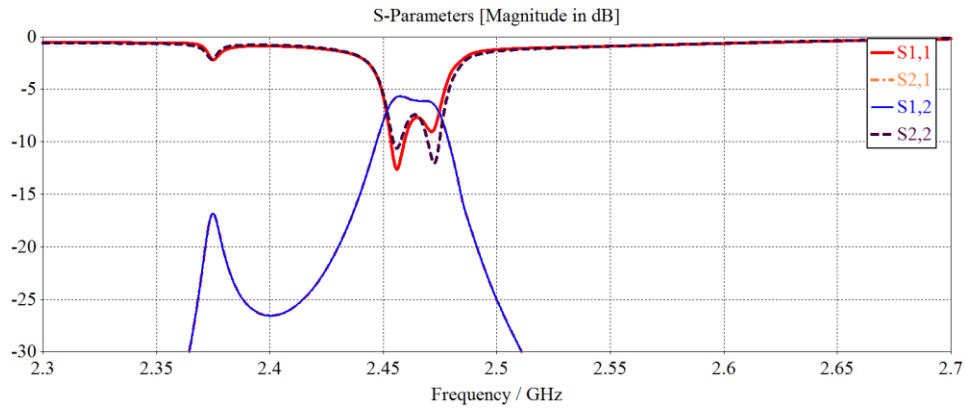
Fig 5-6: Reflection and transmission coefficients of filter ports with presence of antenna ports
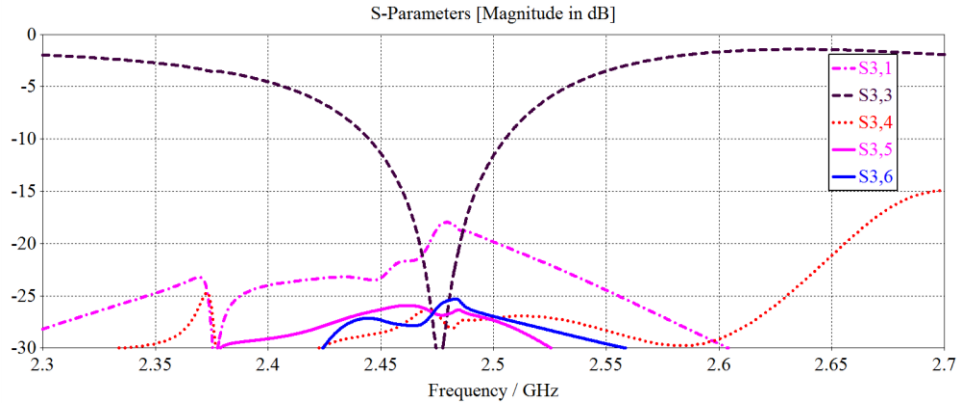
Fig 5-7: first DR $TM_{01\delta}$ mode reflection and coupling coefficients with other ports

The S parameters of port 4 in Fig. 5-8 present the antenna performance of $HEM_{11\delta}$ mode of element 1. The 10dB impedance matching bandwidth is 1.154% (28.24MHz) with less than 26dB reflections at resonance. This port also has less than 25dB couplings with other antennas and about 12dB couplings with filter ports as it was observed in the single element case also.

This strong coupling is introduced by the patches underneath the resonators which is closely located to the microstrip lines that excite $TE_{01\delta}$ modes.
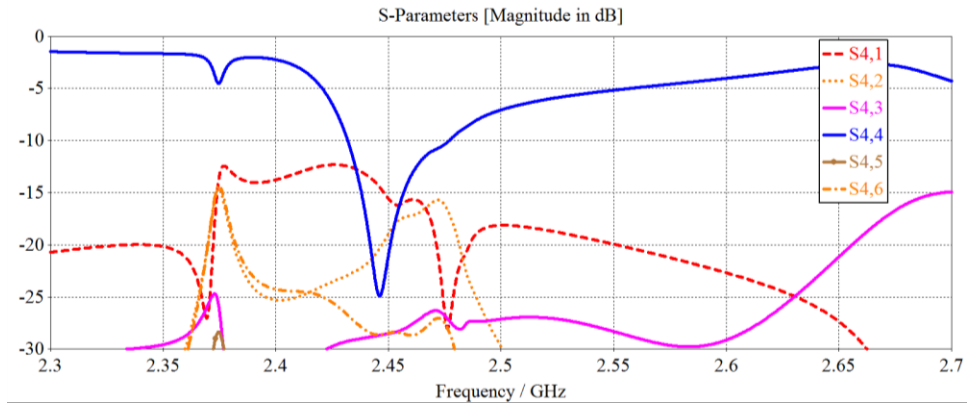
Fig 5-8: first DR $HEM_{11\delta}$ mode reflection and coupling coefficients with other ports
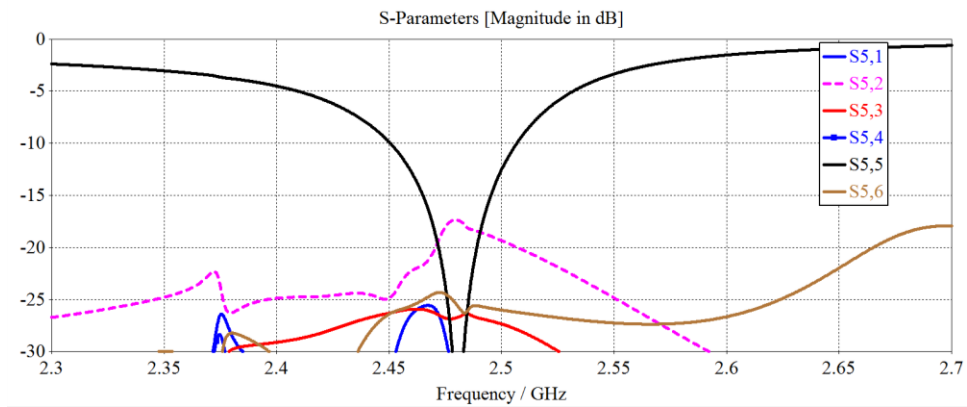
Fig 5-9: second DR $TM_{01\delta}$ mode reflection and coupling coefficients with other ports
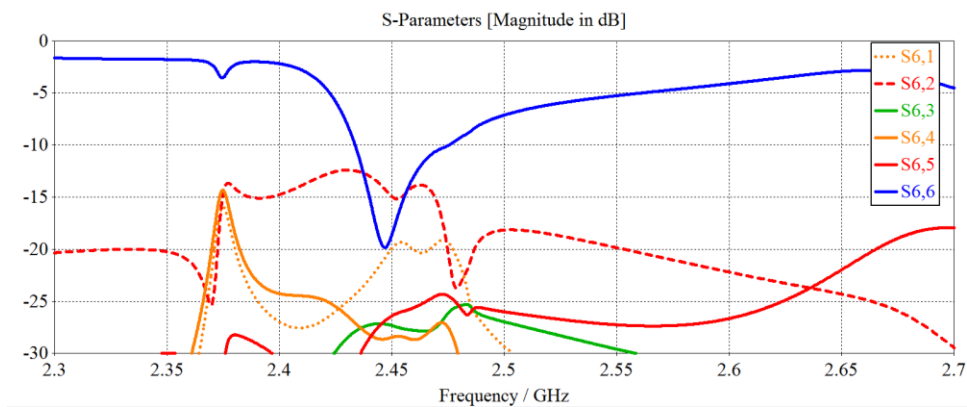
Fig 5-10: second DR $HEM_{11\delta}$ mode reflection and coupling coefficients with other ports

Similarly, the antenna ports of the second element, port 5 for $TM_{01\delta}$ mode and port 6 for $HEM_{11\delta}$ has a lower coupling with the antenna ports. Port 5 has 2.57% (63MHz) and port 6 has 1.2% (26.87MHz) 10dB impedance matching bandwidth presented in Fig. 5-9 and 5-10.

All six port return loss, including filter insertion loss, is represented in Fig. 5-11 to have a clear idea about the operating frequencies of all the modes. It is observed that for all four antenna ports, matching bandwidth coverage is from 2.43GHz to 2.46GHz, which is 1.2% of the operating frequency. Filter insertion loss is about 5.6dB at this range with 13dB matching. The simulated results of CST Frequency domain solver are verified with HFSS presented in Fig. 5-12. Both results showed good agreement for the filter as well as for antennas.
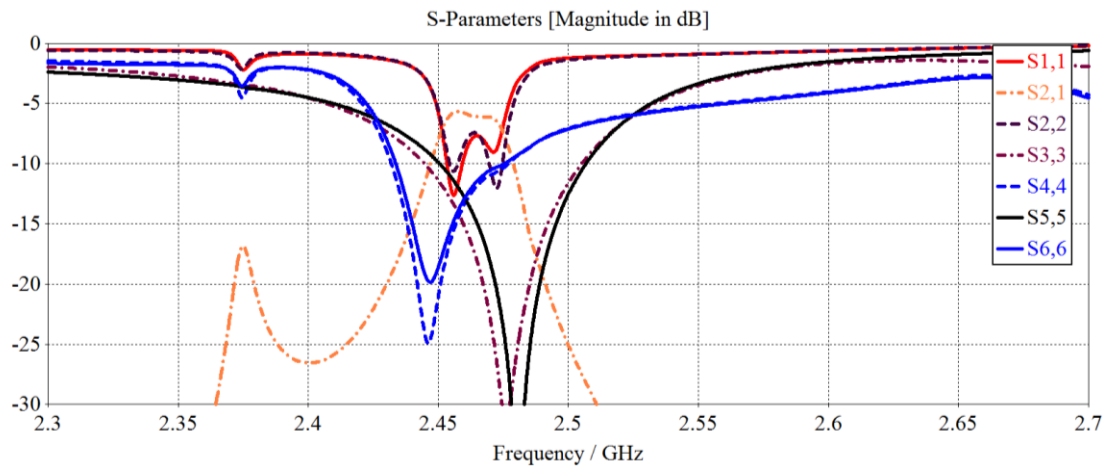
Fig 5-11: return loss of six ports and insertion loss of filter
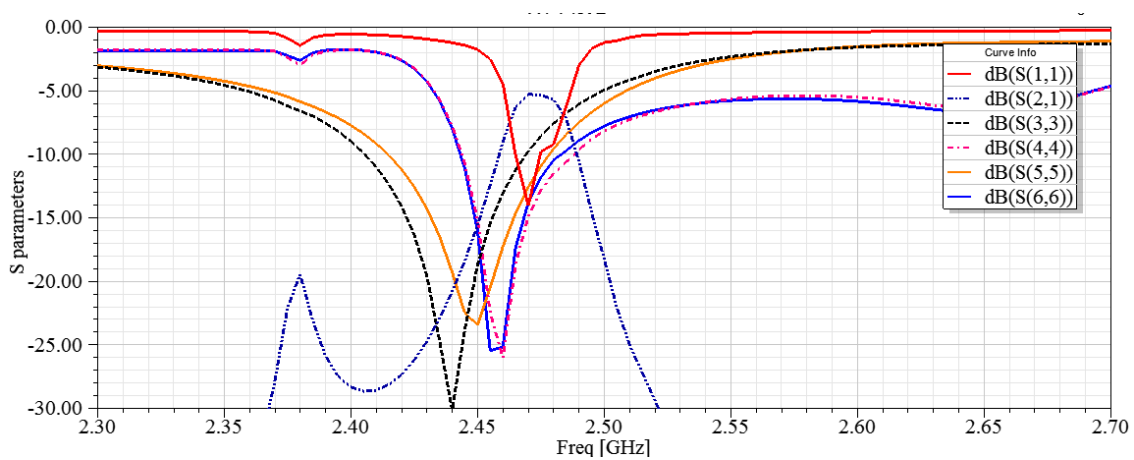
Fig 5-12: return loss of six ports and insertion loss of filter from HFSS

The radiation patterns of the antenna ports are displayed in Fig. 5-13. Omnidirectional radiation patterns are obtained from port 3 and 5 $TM_{01\delta}$ modes whereas broadside patterns are found from port 4 and 6 $HEM_{11\delta}$ modes. $TM_{01\delta}$ mode patterns show the null at broadside, and $HEM_{11\delta}$ mode patterns have a maximum gain at broadside. For $HEM_{11\delta}$ modes, XZ is the E plane, and YZ is the H plane of the patterns. The radiation efficiency and directivity of the omnidirectional antennas of port 3 and 5 are 3.13dB, 95%, and 3.62dB, 95% respectively. On the other hand, for broadside pattern antennas radiation efficiency and directivity of port 4 and 6 are 6.35dB, 90%, and 5.35dB, 90% respectively. It is also good to mention that the TM modes radiation patterns are affected by the TE modes. It is because the filter insertion losses are not maximum which indicates that some radiation might happens from these TE modes. As both the TE and TM modes are axially symmetric, therefore the pattern of TM modes might be affected by the radiation caused by TE modes.

$TM_{01\delta}$ at port 3 $HEM_{11\delta}$ at Port 4

$TM_{01\delta}$ at Port 5 $HEM_{11\delta}$ at Port 6
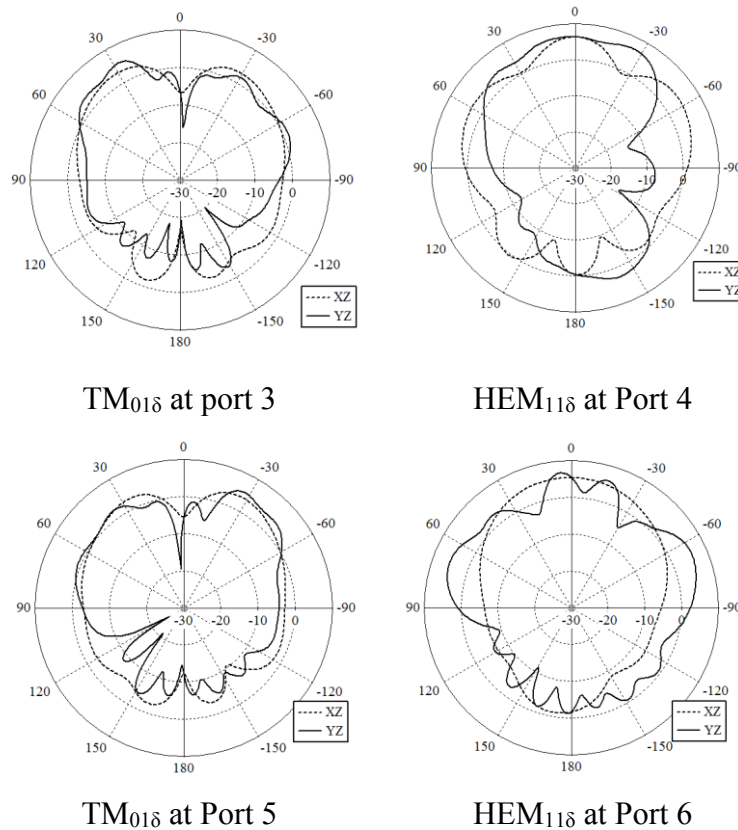
Fig 5-13: radiation patterns of the antenna ports of orthogonal DRs

In order to transmit and receive simultaneously as independent antennas, the correlation between the antennas should be low. As the antennas in the design have same polarization and radiation pattern these antennas have to be appropriately spaced so that they don't interfere with each other. The distance from one resonator center to another resonator center is about $6*\lambda_g$ at the operating frequency which dictates much spacing between them. The envelop correlation coefficient (ECC) is calculated among the antennas from the S parameters is given in Fig. 5-14 that shows very low correlation at 2.45GHz.
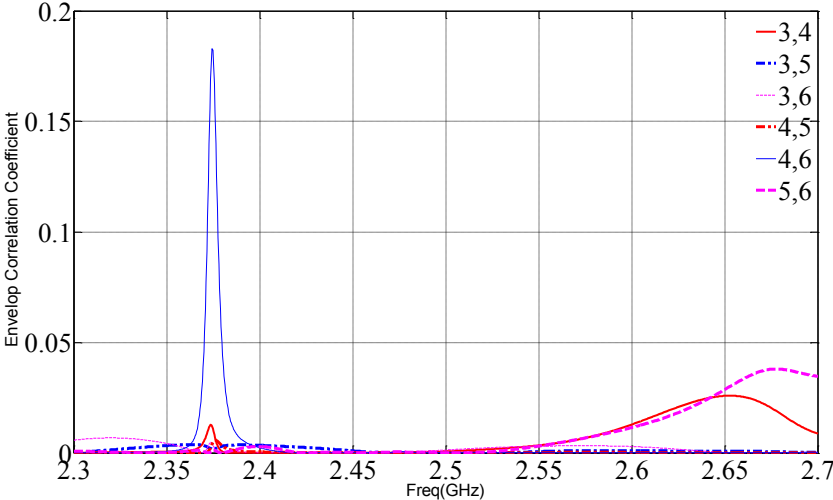
Fig 5-14: Correlation coefficients between antenna ports for asymmetric DRs

5.2.1 Symmetric alignments of two DRs

The second solution consists of two dielectric resonators of the same orientation with the S shape coupling line for the filter. Therefore, the feeding network of the second element also assigned as the first element. Fig. 5-15 shows the coupling network for the antenna ports. Here also port 3, 4 belong to the first element and port 5, 6 belongs to the second element.
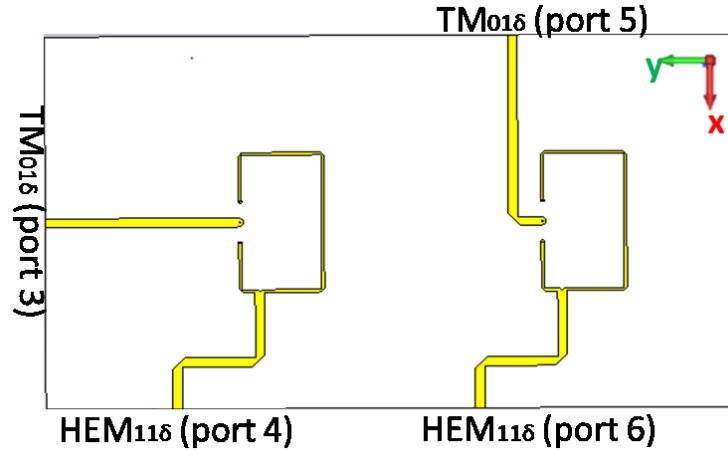
Fig 5-15: Top view of bottom substrate layer for symmetric configuration

The S parameters of the filter ports with the loading effect of antenna ports are given in Fig. 5.16 that indicates almost the same behavior without assigning antenna ports. As the filter ports do not see much variation because of the almost symmetric structure, therefore the loading effect is minimized. The impedance matching is 18dB, and insertion loss is 6.5dB for both port 1 and 2.
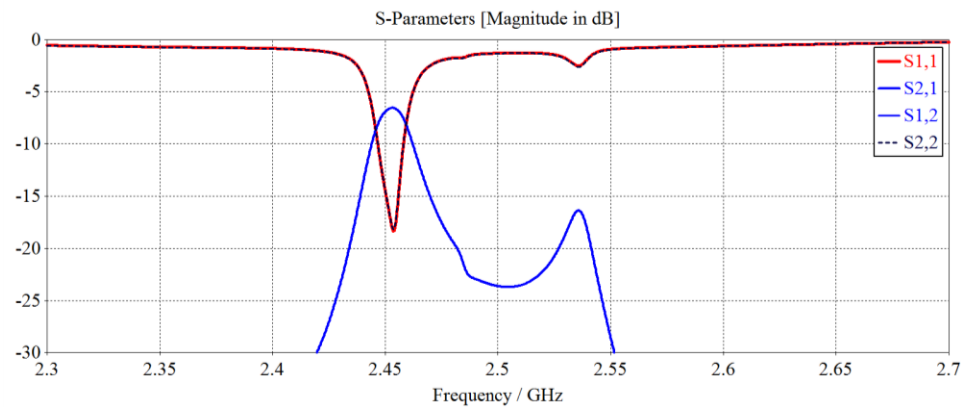
Fig 5-16: Reflection and transmission coefficients of filter ports with presence of antenna ports

Fig. 5-17 to 5-20 presents the reflection at the antenna ports and the coupling between the antennas. $TM_{01\delta}$ mode of port 3 has 2.38% (58.5MHz) 10dB impedance matching bandwidth and 28dB return loss at the resonance. Coupling with all other ports is less than 20dB. For the $HEM_{11\delta}$ mode, port 4 matching bandwidth is 1.52% (37.2MHz) with 18dB return loss. Although Port 4 has less than 25dB couplings with the antenna ports, it has about 16dB coupling with filter ports.
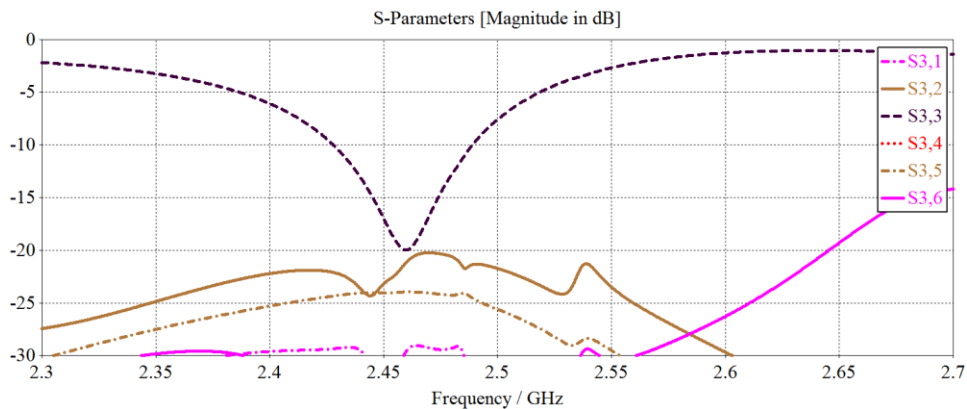
Fig 5-17: Port 3 $TM_{01\delta}$ mode reflection and coupling coefficients with other ports
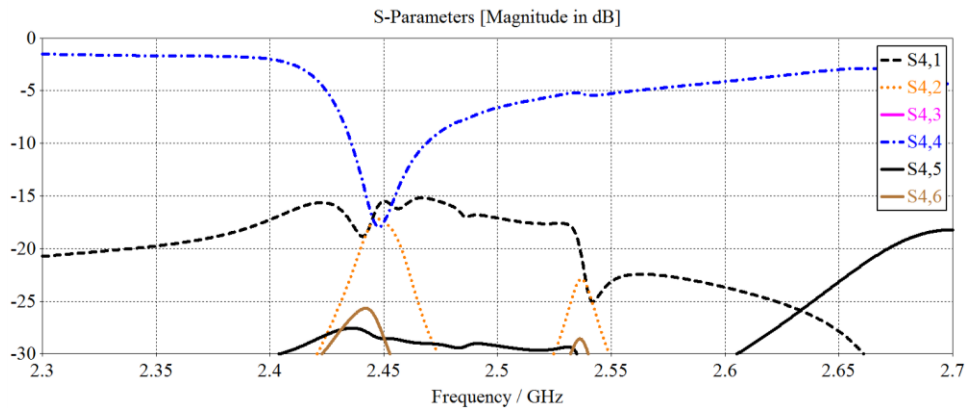
Fig 5-18: Port 4 $HEM_{11\delta}$ mode reflection and coupling coefficients with other ports

The S parameters of $TM_{01\delta}$ mode at Port 5 are almost identical to port 3 as expected. Similarly, $HEM_{11\delta}$ modes of both ports 4 and 6 have the same response.
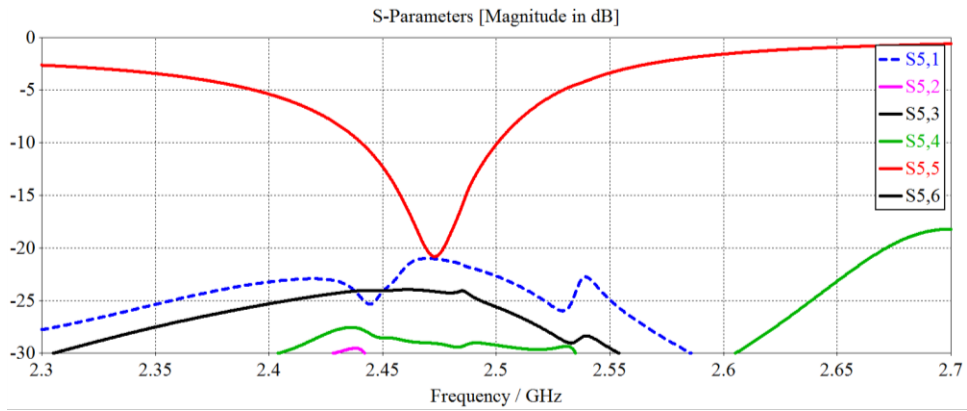
Fig 5-19: Port 5 $TM_{01\delta}$ mode reflection and coupling coefficients with other ports
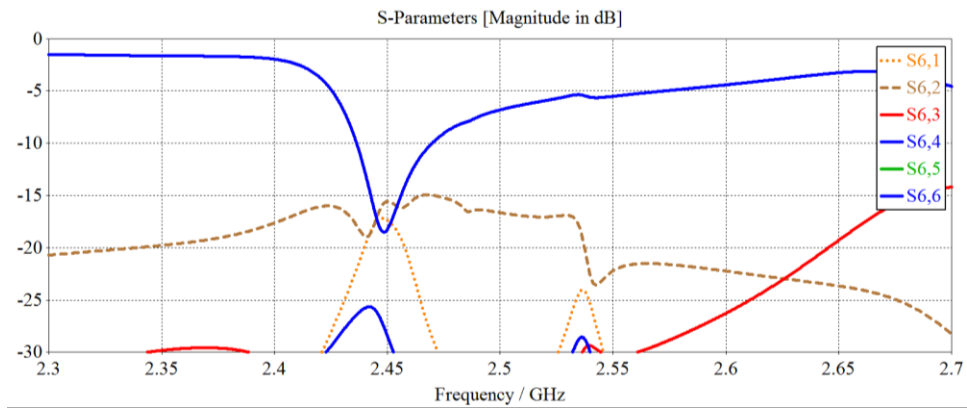
Fig 5-20: Port 6 $HEM_{11\delta}$ mode reflection and coupling coefficients with other ports
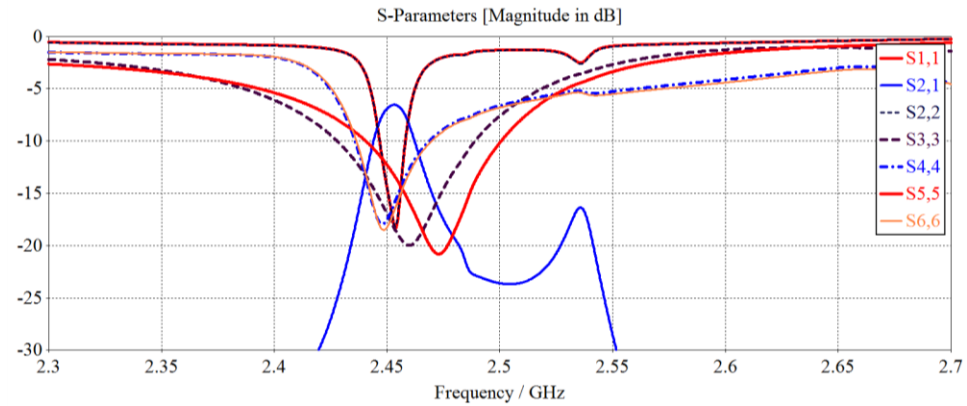
Fig 5-21: return loss of six ports and insertion loss of filter for symmetrically oriented DRs

TM$_{01\delta}$ at port 3   HEM$_{11\delta}$ at Port 4

TM$_{01\delta}$ at port 5   HEM$_{11\delta}$ at Port 6
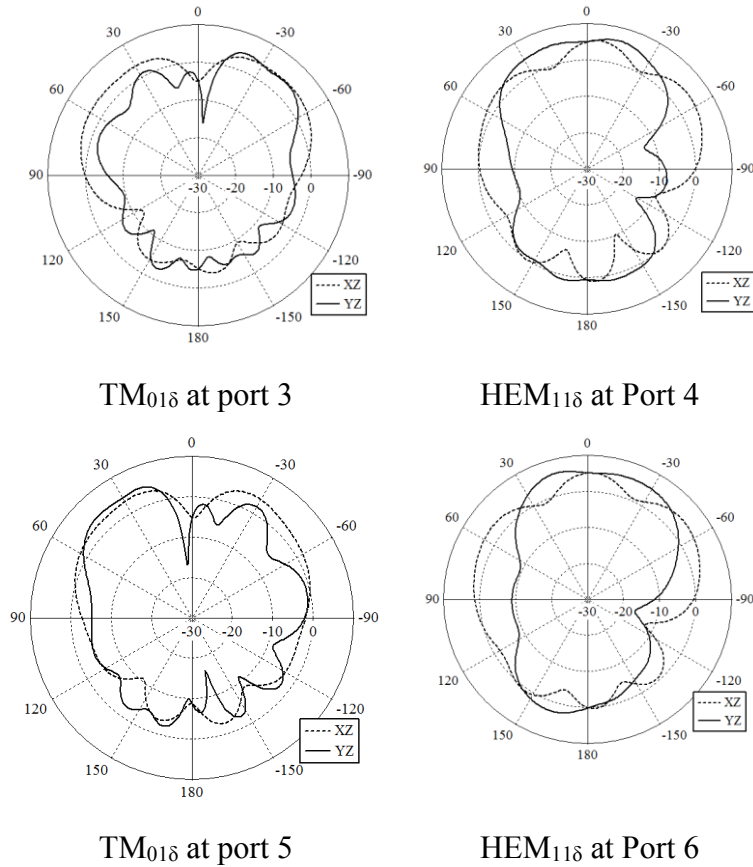
Fig 5-22: radiation patterns of the antenna ports of symmetrical DRs

Fig. 5-21 displays return loss of all six ports with the insertion loss of the filter. At least 18dB return loss can be noticed for all the ports that dictate good matching of the feeding networks. The total bandwidth covered by the antennas is about 40MHz which is appropriate for MIMO. There is no asymmetry between filter ports, and the insertion loss is 6.5dB.

Radiation patterns of the antenna ports are given in Fig. 5-22. Both on port 3 and 5 TM$_{01\delta}$ modes have omnidirectional patterns with a null at θ=0. Although the XZ plane patterns are same for both ports, YZ plane patterns are mirrored to each other. For HEM$_{11\delta}$ modes of port 4 and 6, XZ plane is the E plane, and YZ plane is the H plane. The E plane pattern is almost similar for both ports. On the other hand, a small difference is found in H planes. The directivity obtained for omnidirectional antennas are 3.97dBi and 3.91dBi for port 3 and 5 respectively. For broadside pattern antennas of port 4 and 6, directivities are 5.38dBi and 5.14dBi respectively.

The envelop correlation coefficients between the antenna ports are calculated from the S parameters are presented in 5-23. These shows almost zero correlation between the antennas. In this design, the distance between one resonator center to another resonator center is about $4*\lambda_g$ which is enough space to have an independent operation of the antennas.
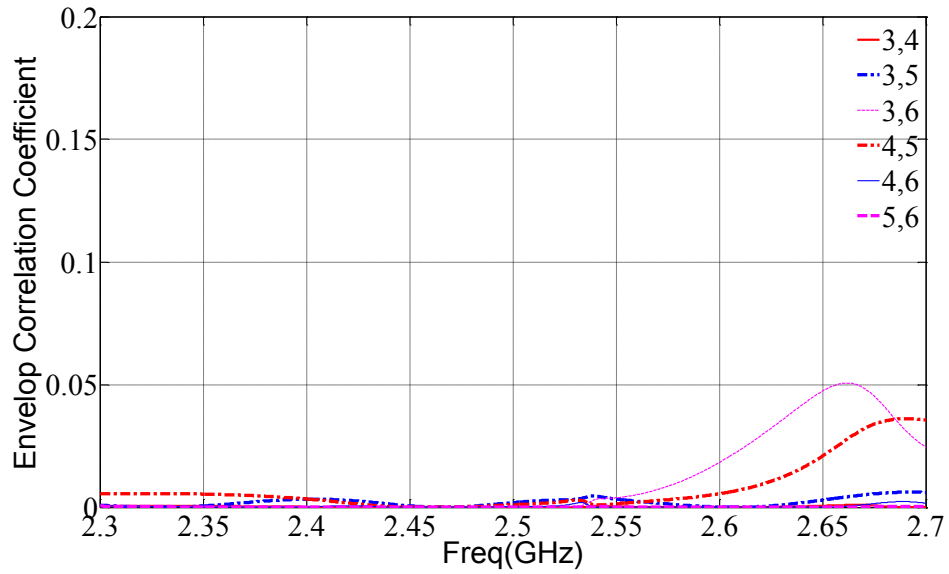
Fig 5-23: Correlation coefficients between antenna ports for symmetric DR

5.3 Characteristics of both designs

Two elements placed orthogonally:

- The insertion loss is about 5.6dB with 8dB matching
- The distance between the resonators is much longer. Therefore, the structure is big
- The distance is chosen for the better insertion loss of the filters which can be shorter without a filter. This will make the design compact for MIMO antennas. However, the antennas will perform independently as the elements are orthogonal.
- The orthogonal orientation of the DRs dictates polarization variety
- There is an asymmetry between the filter ports because of the orthogonal position of the slots on top metal.
- The loading effect of antenna ports is higher on the filter matching performance.
- The minimum matching bandwidth covered by all antennas is 30MHz

Two elements placed symmetrically:

- Filter matching is 19dB with 6.5dB insertion loss
- There is no asymmetry between the filter ports.
- The loading effect of antenna ports on filter ports is minimized
- The resonators are comparatively close to each other which gives a compact size for MIMO antennas with a reasonable filter performance
- As the modes of resonators are similarly polarized, it is essential to keep a longer spacing even without the filter.
- The minimum matching bandwidth covered by all antennas is 40MHz

Chapter 6
Conclusion and Future Work

The motivation of the thesis to tune the resonant frequencies of lower order modes of a cylindrical DRA by using the perturbation technique is explained initially. The necessity of such a DRA for the multifunctional device is also presented with some examples of related literature. The main contribution of this thesis is the observation of geometric perturbation technique to tune the resonant frequencies of different modes. The cavity perturbation formulas are used to obtain the response of small perturbation whereas it has also been mentioned that for the more significant reduction area the cavity perturbation equations provide less accuracy in assuming resonant frequencies. The detail of the perturbation procedure is presented incorporated with field and energy distributions of the modes. The importance of metallic shielding is mentioned to obtain better impedance matching for the $TE_{01\delta}$ mode. In addition, to mitigate the effect of the metallic shield on other modes another perturbation is performed at the top part of the resonator. The effect of normalized perturbation parameters on normalized resonant frequencies of different modes is provided graphically. It has been clearly observed that it is possible to obtain the three lowest order modes $TE_{01\delta}$, $TM_{01\delta}$, and $HEM_{11\delta}$ at the same frequency through the illustrated geometric perturbation technique. Furthermore, some additional methods of geometric perturbation of different dielectric constant resonators are also shown to obtain three modes together at the same frequency.

The perturbation concept described in chapter 3 has been implemented in designing a multi-functional dielectric resonator device where the $TE_{01\delta}$ mode is used as a filter element, $TM_{01\delta}$ as an omnidirectional pattern antenna and $HEM_{11\delta}$ is utilized to obtain a broadside pattern antenna. The feeding mechanism of this four port device incorporating two substrate layers is provided individually in chapter 4. Several difficulties have been found to fulfill the engineering requirements of the designed prototype, especially combining multiple slices of the dielectric material to have one single DR element that introduced air gap. Also, the conducting vias to connect the patches on the top layer substrate with microstrip lines at the bottom layer to feed the $HEM_{11\delta}$ mode was very challenging. In addition, the insertion of the probe in the center of the

dielectric resonator while maintaining the contact with a circular patch to excite the $TM_{01\delta}$ mode needed much longer time and attention.

Despite the fabrication challenges, the built prototype measurement results showed good agreement with the simulated results except for some frequency shifts due to the air gap. The simulated and measured impedance matching of four ports and the coupling coefficients between them are well performed, and the radiation patterns of the antenna elements are also behaving as required. The filter impedance matching is 20dB with 1.41 dB insertion loss. The 10 dB impedance matching the bandwidth of the omnidirectional antenna is 3.11% at 2.41 GHz, and for broadside pattern antenna it is 1.083% at 2.3 GHz while achieving good matching performance. In addition, the calculated low correlation coefficient of the antennas is provided to prove the adaptability of this device in a MIMO environment.

As per IEEE 802.11n maximum, four antennas can be implemented to obtain better MIMO performance. Therefore, to achieve maximum MIMO performance, two single elements are cascaded to obtain four antennas where a coupling line is placed in between DRs for a bandpass filter. Although filter performance is not acceptable here, the antennas worked very well.

This work can be extended in future to obtain several advantages:

Utilizing higher order modes: The perturbation concept described here considered only three lowest order modes of the dielectric resonator. The similar concept can also be applied to tune the higher order modes which have different characteristics.

GPS application: The antennas for GPS application require having a circular polarization which can be generated by perturbing the structure to obtain orthogonal degenerated modes. Once the perturbed resonating structure provides these orthogonal modes, it can be easily coupled to the external feeding network to get circular polarization.

Different functions: In this work, the dual function of a DR is presented as filter and antennas. Several other applications can be obtained from the DR such as a diplexer, duplexer, and higher order filters, etc.

5G applications: As the frequency of 5G is high, therefore smaller devices are required. As the DR wavelength is a function of dielectric constant, therefore high ε_r materials can be used to design 5G devices.

The proposed perturbation concept is presented to obtain multiple modes at a single frequency that can be utilized to design a multi-functional device. As the modern technology has rigorously developed, ideas are needed to work at millimeter wavelengths. Therefore, the downsizing of the devices is a significant factor that requires a single device with multiple functions. Hence, the geometric perturbation technique of dielectric resonator can be a useful tool to design such devices.

Bibliography

[1] T. Rappaport, *Wireless Communications: Principles and Practice.*, Prentice Hall, 2001.

[2] D. Gesbert, M. Shafi, Da-shan Shiu, P.J. Smith, A. Naguib, "From theory to practice: an overview of MIMO space-time coded wireless systems," *IEEE Journal on Selected Areas in Communications, Volume: 21, Issue: 3, Apr.* 2003.

[3] M. A. Jensen and J. W. Wallace, "A review of antennas and propagation for MIMO wireless communications," *IEEE Transactions on Antennas and Propagation, Vol. 52, No. 11, November* 2004.

[4] D. T. Lizhong Zheng, "Diversity and multiplexing: a fundamental tradeoff in multiple-antenna channels," *IEEE Transactions on Information Theory, Volume: 49, Issue: 5*, 2003.

[5] R. U. N. Arogyaswami J. Paulraj, Dhananjay A. Gore, and H. Blcskei, "An overview of MIMO communications a key to gigabit wireless," *Proceedings of the IEEE, Volume: 92, Issue: 2, Feb* 2004.

[6] E. W. K. Oscar Bejarano and M. Park, "IEEE 802.11ac: From channelization to multi-user MIMO," *IEEE Communications Magazine, October* 2013.

[7] E. Antonino-Daviu, M. Cabedo-Fabres, M. Gallo, M. Ferrando-Bataller and M. Bozzetti, "Design of a multimode MIMO antenna using characteristic modes," *3rd European Conference on Antennas and Propagation*, 2009.

[8] O. E. Erik G. Larsson, F. Tufvesson, and T. L. Marzetta, "Massive MIMO for next generation wireless systems," *IEEE Communications Magazine, February* 2014.

[9] Tomislav Debogović, Pedro Robustillo-Bayon, Nevena Šaponjic, Frédéric Bongard, Marco Sabbadini, Ferdinando Tiezzi and Juan R. Mosig, "Low-profile multi-function antenna system for small satellites," in *10th European Conference on Antennas and Propagation (EuCAP)*, 2016.

[10] L. K. Hady, D. Kajfez, and A. A. Kishk, "Triple mode use of a single dielectric resonator," *IEEE Transactions on Antennas and Propagation*, vol. 57, no. 5, pp. 1328–1335, May 2009.

[11] David M. Pozar, "*Microwave Engineering*" 4th, Ed., John Wiley & Sons, Inc.

[12] A. Gorur and C. Karpuz, "Miniature dual-mode microstrip filters," *IEEE Microwave and Wireless Components Letters, Volume: 17, Issue: 1, Jan.* 2007.

[13] P. Guillon, Y. Garault, J. Farenc P, "Dielectric resonator dual modes filter," *Electronics Letters, Volume: 16, Issue: 17, August 14*, 1980.

[14] J.B. Yan and J. T. Bernhard, "Design of a MIMO dielectric resonator antenna for LTE femtocell base stations," *IEEE Transactions on Antennas and Propagation, Volume: 60, Issue: 2, Feb.* 2012.

[15] K. M. Luk and K. W. Leung, "Dielectric Resonator Antennas." England, Hertfordshire Research Studies Press Ltd., 2003.

[16] A. Petosa, "Dielectric Resonator Antenna Handbook." Norwood, MA, Artech House, 2007.

[17] S. B. Cohn, "Microwave bandpass filters containing high-Q dielectric resonators," *IEEE Transactions on Microwave Theory and Techniques, Volume: 16, Issue: 4*, 1968.

[18] M. M. S. Long and L. Shen, "The resonant cylindrical dielectric cavity antenna," *IEEE Transactions on Antennas and Propagation, Volume: 31, Issue: 3, May* 1983.

[19] A. Petosa and A. Ittipiboon, "Dielectric resonator antennas: A historical review and the current state of the art," *IEEE Antennas and Propagation Magazine, Volume: 52, Issue: 5, Oct.* 2010.

[20] R. K. Mongia and P. Bhartia, "Dielectric resonator antennas-a review and general design relations for resonant frequency and bandwidth," *International Journal of Microwave and Millimeter-Wave Computer-Aided Engineering, vol. 4, no. 3, pp. 230-247*, 1994.

[21] R. R. Mansour, "High-Q tunable dielectric resonator filters," *IEEE Microwave Magazine, 10, 6, Oct.* 2009.

[22] S. Fiedziuszko and R. Chapman, "Miniature filters and equalizers utilizing dual mode dielectric resonator loaded cavities," in *IEEE MTT-S International Microwave Symposium Digest*, 1982.

[23] T. Nishikawa, K. Wakino, H. Wada, and Y. Ishikawa, "800 MHz band dielectric channel dropping filter using TM/sub 110/ triple mode resonance," in *IEEE MTT-S International Microwave Symposium Digest*, 1985.

[24] L. K. Hady, D. Kajfez and A. A. Kishk, "Dielectric resonator antenna in a polarization filtering cavity for dual function applications," *IEEE Transactions on Antennas and Propagation, VOL. 56, NO. 12, December* 2008.

[25] Longfang Zou, Derek Abbott, and Christophe Fumeaux, "Omnidirectional cylindrical dielectric resonator antenna with dual polarization," *IEEE Transactions on Antennas and Propagation Letters, VOL. 11*, 2012.

[26] E. H. Lim and K. W. Leung, "Novel application of the hollow dielectric resonator antenna as a packaging cover," *IEEE Transactions on Antennas and Propagation, Volume: 54, Issue: 2, Feb.* 2006.

[27] E. H. Lim, K. W. Leung, "Use of the dielectric resonator antenna as a filter element," *IEEE Transactions on Antennas and Propagation, 56, 1, January* 2008.

[28] L. K. Hady, D. Kajfez and A. A. Kishk, "Dual-band compact DRA with circular and monopole-like linear polarizations as a concept for GPS and WLAN applications," *IEEE Transactions on Antennas and Propagation,57, 9, September* 2009.

[29] M. Memarian and R. Mansour, "Quad-mode and dual-mode dielectric resonator filters," *IEEE Transactions on Microwave Theory and Techniques, 57, 12, Dec.* 2009.

[30] Taomia. T. Pramiti, M. A. Moharram, A. Kishk, "Geometry perturbation of dielectric resonator for same frequency operation as radiator and filter," *Accepted at URSI General Assembly and Scientific Symposium (GASS)*, 2017.

[31] S. K. Chatterjee, "Microwave cavity resonators some perturbation effects and their applications," *Journal of the British Institution of Radio Engineers*, 1953.

[32] Y. Shu, T.Y. Wong, "Perturbation of dielectric resonator for material measurement," *Electronics Letters, Volume: 31, Issue: 9, 27 Apr* 1995.

[33]   David G. Santiago, G. John Dick and Aluizio Prata, "Mode Control of Cryogenic Whispering-Gallery Mode Sapphire Dielectric-Ring Resonators," *IEEE Transactions on Microwave Theory and Techniques, VOL. 42, NO. 1, January* 1994.

[34]   Wen-Hua Tu and Kai Chang, "Piezoelectric Transducer-Controlled Dual-Mode Switchable Bandpass Filter," *IEEE Microwave and Wireless Components Letters, Volume: 17, Issue: 3*, 2007.

[35]   S. W. Wong, Z. C. Zhang et al., "Triple-Mode Dielectric Resonator Diplexer for Base-Station Applications," *IEEE Transactions on Microwave Theory and Techniques, Volume: 63, Issue: 12, Dec.* 2015.

[36]   K. S. Ryu and A. A. Kishk, "Ultrawideband Dielectric Resonator Antenna with Broadside Patterns Mounted on a Vertical Ground Plane Edge," *IEEE Transactions on Microwave Theory and Techniques, VOL. 58, NO. 4, April* 2010.

[37]   H. Gajera, D. Guha and C. Kumar, "New technique of dielectric perturbation in dielectric resonator antenna to control the higher mode leading to reduced cross-polar radiations," *IEEE Antennas and Wireless Propagation Letters, Vol. 16*, 2017.

[38]   M. H. Jamaluddin, R. Gillard, R. Sauleau and Marie-Anne Milon, "Perturbation Technique to Analyze Mutual Coupling in Reflectarrays," *IEEE Transactions on Microwave Theory and Techniques, VOL. 8*, 2009.

[39]   K. Ishimiya, J. Langbacka et al., "A Compact MIMO DRA Antenna," *Proc. IEEE Int. Workshop on Antenna Technology: Small Antennas and Novel Metamaterials (IWAT '08)*, 2008.

[40]   A. Dadgarpour, B. Zarghooni et al., "Mutual Coupling Reduction in Dielectric Resonator Antennas using Metasurface Shield for 60-GHz MIMO Systems," *IEEE Antennas and Wireless Propagation Letters, Volume: 16*, 2016.

[41]   R. Tian, V. Plicanic et al., "A compact six-port dielectric resonator antenna array: MIMO Channel Measurements and Performance Analysis," *IEEE Transactions on Antennas and Propagation, Volume: 58, Issue: 4, April* 2010.

[42] L. Huitema, M. Koubeissi et al., "Compact and Multiband Dielectric Resonator Antenna with Pattern Diversity for Multistandard Mobile Handheld Devices," *IEEE Transactions on Antennas and Propagation, VOL. 59, NO. 11, November* 2011.

[43] L. Thamae and Z. Wu, "Dielectric Resonator-Based Multiple-Input Multiple Output Antennas and Channel Characteristic Analysis," *Published in IET Microwaves, Antennas & Propagation, March* 2012.

[44] Lei Zhong, Jing-Song Hong and Hong-Cheng Zhou, "A Novel Pattern-Reconfigurable Cylindrical Dielectric Resonator Antenna with Enhanced Gain," *IEEE Antennas and Wireless Propagation Letters, Volume: 15, November* 2015.

[45] Mohamed T. Hussain, Mohammad S. Sharawi et al., "Closely Packed Millimeter-Wave MIMO Antenna Arrays with Dielectric Resonator Elements," *10th European Conference on Antennas and Propagation (EuCAP)*, 2016.

[46] Dr. J. L. Volakis, "Antenna Engineering Handbook"*,* chapter 17. The McGraw-Hill Companies, 2007.

[47] CST STUDIO SUITE (2017). DS SIMULIA [Online]. Available: http://www.cst.com

[48] P. Guillon, B. Byzeryand M. Chaubet, "Coupling Parameters between A Dielectric Resonator and a Microstrip line," *IEEE Transactions on Microwave Theory and Techniques, Vol. 33, No. 3, March* 1985.

[49] David M. Pozar, "*Microwave Engineering*" 4th Ed., 308, John Wiley & Sons, Inc

[50] S. Blanch, J. Romeu and I. Corbella, "Exact representation of antenna system diversity performance from input parameter description*," Electronics Letters, Vol: 39, Issue: 9, 1 May 2003*